



Methods for characterising the steel–concrete interface to enhance understanding of reinforcement corrosion: a critical review by RILEM TC 262-SCI

Hong S. Wong · Ueli M. Angst · Mette R. Geiker · O. Burkan Isgor · Bernhard Elsener · Alexander Michel · Maria Cruz Alonso · Maria Joao Correia · Jose Pacheco · Joost Gulikers · Yuxi Zhao · Maria Criado · Michael Raupach · Henrik Sørensen · Raoul François · Shishir Mundra · Mezgeen Rasol · Rob Polder

Received: 20 January 2022 / Accepted: 8 April 2022 / Published online: 3 May 2022
© The Author(s) 2022

Abstract The steel–concrete interface (SCI) is a complex, multi-phase and multi-scale system. It is widely known to influence the performance and long-term durability of concrete structures. However, a fundamental understanding of its properties and effects on corrosion initiation of embedded reinforcing steel remains elusive. This is attributed to its complicated heterogeneity and time-dependent nature, exacerbated by the lack of suitable techniques for systematic and detailed characterisation. This paper,

prepared by members of the RILEM Technical Committee 262-SCI, critically reviews available information regarding current methods (laboratory or field-based) for characterising local properties of the SCI that have been identified as governing factors affecting corrosion initiation. These properties include characteristics of the steel such as mill scale and rust layers, and characteristics of the concrete such as interfacial voids, microstructure and moisture content. We evaluated over twenty methods and summarised

This article has been prepared within a framework of RILEM TC 262-SCI. The article has been reviewed and approved by all TC members.

TC Membership.

Chair: Ueli M. ANGST.

Deputy Chair: Mette R. GEIKER.

TC Members: Mark G. Alexander, Ueli Angst, Maria Joao Correia, Maria Criado, Maria Cruz Alonso, Bernhard Elsener, Raoul François, Christoph Gehlen, Mette Geiker, Arpit Goyal, Joost Gulikers, Carolyn Hansson, Karla Hombostel, O. Burkan Isgor, David Law, Andraz Legat, Kefei Li, Victor Marcos Meson, Alexander Michel, Shishir Mundra, Mike B. Otieno, José Pacheco, Radhakrishna Pillai, Rob Polder, Mezgeen Rasol, Michael Raupach, Alberto A Sagüés, Henrik Erndahl Sørensen, Luping Tang, Elsa Vaz Pereira, Talakokula Visalakshi, Junjie Wang, Hong S. Wong, Linwen Yu, Zhidong Zhang; and Yuxi Zhao.

H. S. Wong (✉)
Department of Civil and Environmental Engineering,
Imperial College London, London SW7 2AZ, UK
e-mail: hong.wong@imperial.ac.uk

U. M. Angst · B. Elsener · S. Mundra
Institute for Building Materials (IfB), ETH Zurich,
Stefano-Franscini-Platz 3, 8093 Zurich, Switzerland

M. R. Geiker
Department of Structural Engineering, Norwegian
University of Science and Technology, 7491 Trondheim,
Norway

O. B. Isgor
School of Civil and Construction Engineering, Oregon
State University, Corvallis, OR, USA

A. Michel
Department of Civil Engineering, Technical University of
Denmark (DTU), 2800 Kgs. Lyngby, Denmark



their advantages, applications and limitations. The findings show a severe lack of well established, non-destructive techniques that are suitable for direct monitoring of the SCI at a representative scale with sufficiently high resolution (spatial, temporal), particularly for moisture related aspects. Several promising novel techniques with significant potential for further development and application were identified and discussed. Finally, we provide several recommendations for future research needs that are required to advance this critically important topic.

Keywords Steel–concrete interface · Durability · Corrosion · Microstructure · Moisture · Characterisation

1 Introduction

It is well known that the steel–concrete interface (SCI) plays a significant role in determining the performance and long-term durability of reinforced concrete structures. Yet, our fundamental understanding of the SCI is incomplete. Recent state-of-the-art reviews, prepared by the members of RILEM TC 262-SCI, attempted to elucidate the characteristics of the SCI and their potential impact on corrosion of steel

reinforcement in concrete [1, 2]. These reviews have shown that, despite many decades of research, the most dominant SCI characteristics influencing the susceptibility of steel reinforcement to corrosion remain largely unclear.

The associated uncertainty is mainly attributed to the complexity and heterogeneity of the SCI, and its interactions with many factors. However, the absence of a comprehensive understanding and the existence of (some) conflicting findings in the literature are also, to an extent, due to a lack of informative, consistent and well-established experimental methods for studying the SCI. This limits our ability to model reinforcement corrosion accurately, formulate new materials and construction practices to build corrosion-resistant reinforced concrete structures, and develop new means and methods to delay corrosion onset or propagation, extending the service life of existing structures. Thus, a systematic approach for characterising the local, physical, and chemical properties of the SCI is highly needed.

The overall aim of this paper is to evaluate techniques for characterising local properties of the SCI that have been identified as the main factors influencing corrosion initiation in previous publications by the RILEM TC 262-SCI. These include characteristics of the steel surface such as mill scale

M. C. Alonso · M. Criado
Institute of Construction Science Eduardo Torroja-CSIC,
Serrano Galvache 4, 28033 Madrid, Spain

M. J. Correia
National Laboratory for Civil Engineering, Materials
Department, Av. Do Brasil 101, 1700-066 Lisbon,
Portugal

J. Pacheco
CTL Group, Skokie, IL, USA

J. Gulikers
Ministry of Infrastructure and Water Management,
Rijkswaterstaat-GPO, Griffioenlaan 2, 3526,
LA, Utrecht, The Netherlands

Y. Zhao
Institute of Structural Engineering, Zhejiang University,
Hangzhou 310058, China

M. Raupach
Institute of Building Materials Research, RWTH Aachen
University, Schinkelstrsse 3, 52056 Aachen, Germany

H. Sørensen
Concrete Centre, Danish Technological Institute (DTI),
Gregersensvej, 2630 Taastrup, Denmark

R. François
LMDC, INSA, UPS, Université de Toulouse, Toulouse,
France

M. Rasol
MAST/EMGCU, Université Gustave Eiffel, 5 Boulevard
Descartes, 77454 Marne-la-Vallée cedex 2, France

R. Polder
RPCP, Gouda, The Netherlands



and rust layers, and characteristics of the concrete such as interfacial voids, microstructure and moisture content [2]. This paper will focus on techniques currently used in practice (in the laboratory or field) and touch on potential methods under development. Where possible, the paper will provide recommendations on experimental protocols and identify future research needs. Specifically, the paper will address the following questions:

- What are the features of the SCI that currently available techniques can characterise?
- What are these techniques, their performance, and their reliability?
- What can we do with available techniques and the collected data?
- What are the future research needs in terms of enhancing/developing characterisation techniques?

The work should help to guide and improve future studies, which are needed to understand the fundamental mechanisms operative in corrosion initiation of steel in concrete, aid the development of more durable materials, novel test methods, and models for predicting reinforcement corrosion.

2 Methods overview

We have examined over twenty methods in this review. These can be broadly classified according to their working principle and/or analysis method, e.g. microscopy, radiography, tomography, spectroscopy, etc., as listed in Table 1. They can also be categorised according to the scale and location of measurement relative to the SCI, as shown in Fig. 1. The most promising techniques should be capable of providing a direct characterisation of the SCI, either on specific locations at the interface (a), along the interface (b), or around its circumference (c). Some methods may provide information in the form of a distribution profile through the concrete cover, extending to the SCI (d). Other techniques are applicable only to the bulk concrete, steel or reinforced concrete, as a proxy to the SCI (e, f, g, h).

The review is structured according to features of the SCI that have been identified as being the most relevant to corrosion initiation of conventional carbon steel reinforcement in portland cement-based concrete [2]. These are organised and presented in three

themes: (a) mill scale and rust layers (Sect. 3); (b) interfacial voids and concrete microstructure (Sect. 4); and (c) moisture content and spatial distribution (Sect. 5). In each, we provide some background to the main properties and research questions, followed by a critical assessment of the most promising methods. Section 6 reviews other techniques that may yield valuable information but are not necessarily performed directly at the SCI. Finally, we discuss the implications of the review and summarise the main findings.

3 Steel properties: mill scale & rust layer

3.1 Background

It is well established that both corrosion initiation and subsequent propagation are affected by mill scale and pre-existing rust layers on steel surfaces [1]. For example, higher chloride thresholds have been reported for rebars that have been modified through sandblasting, polishing or pickling compared to as-received rebars with mill scale [3–7]. In addition, the removal of these surface layers has been shown to reduce the variability in electrochemical measurements and chloride thresholds [8, 9]. This can be explained by the fact that rebars with cleaned (i.e. modified) surfaces are almost uniform, whereas those in as-received conditions used on-site in concrete structures are locally diverse and complex due to the presence of mill scale or native rust layers [10]. Therefore, it is not practically relevant to focus on corrosion initiation of clean rebars.

Mill scale is a thin, adherent iron oxide coating that forms on rebar during heat treatment and hot rolling processes at the steel mill [1]. Oxidation of the steel occurs after exposure to air while cooling from the rolling temperature. Mill scale is brittle and hence likely to crack during transport, handling (e.g. bending), and placement in the formwork. In terms of morphology and composition, mill scale differs from corrosion products. For example, the mill scale has a higher Fe/O atomic ratio and therefore it is possible to differentiate these layers [11]. At early stages of corrosion, the mill scale is usually found near the outer edge of the solid rust layer as the latter expands from the corroding site.

Table 1 List of methods (ordered according to working principle and/or method of analysis) and features that can be characterised

Method	Features that can be characterised, their location and scale				
	Mill-scale	Rust layer	Interfacial voids	Micro-structure	Moisture
<i>Microscopy</i>					
Optical microscopy (OM)	a, b, c	a, b, c	a, b, c	a, b, c, d	–
Secondary elec. (SEM-SE)	a, b, c	a, b, c	–	a, b, c	–
Backscattered elec. (SEM-BSE)	a, b, c	a, b, c	a, b, c	a, b, c, d	–
Focused ion beam (FIB-SEM)	(a)	(a)	(a)	(a)	–
Transmission elec. (TEM)	(a)	(a)	–	(a)	–
<i>Radiography and tomography</i>					
X-ray imaging (μ CT)	(a, b, c)	(a, b, c)	(a, b, c)	(a, b, c, d)	(d, e, f, g)
Neutron imaging	–	–	(a, b, c)	(a, b, c)	(a, b, c, d)
Combined X and neutron imaging	–	–	(a, b, c)	(a, b, c)	(a, b, c, d)
<i>Spectroscopy</i>					
Energy-dispersive X-ray (EDX)	a, b, c	a, b, c	–	a, b, c, d	–
Raman spectroscopy	a, b, c	a, b, c	–	(a, b, c, d)	–
X-ray photoelectron (XPS)	a	a	–	–	–
Infrared spectroscopy (IR)	–	–	–	–	(e, f, g, h)
<i>Physical</i>					
Nano/micro indentation	a, b, c	a, b, c	–	a, b, c, d	–
Thermogravimetric analysis (TGA)	–	–	–	–	(a, b, c, d) g, h
Dynamic vapour sorption (DVS)	–	–	–	–	(a, b, c, d) g, h
<i>Others (less applicable)</i>					
Electrochemical	e	e	–	–	–
Mass transport based	–	–	d, e	–	–
Electrical resistivity	–	–	–	–	(d, e, f, g, h)
Elec. resistance tomography (ERT)	–	–	–	–	(e, f, g, h)
Ground-penetrating radar (GPR)	–	–	–	–	(e, f, g, h)
Nuclear magnetic res. (NMR)	–	–	–	–	(e, f, g, h)

Letters a, b, c, d, e, f, g and h refer to the location and scale of measurement, as defined in Fig. 1

Parentheses () indicate that the method may potentially be applicable under certain conditions but lacks well-documented evidence

Endash “–” indicates that the method is not applicable

It is well known that voids and crevices exist between the steel and mill scale/rust layers [12]. Some of the voids and crevices are connected by cracks, which serve as pathways for ions in the pore solution to reach the steel through electromigration and diffusion. Thus, the main role of mill scale and rust layers on corrosion initiation can be explained by the crevice corrosion mechanism, illustrated in Fig. 2. Over time, the composition of the solution within the crevices changes from that of the bulk pore solution [12]. Specifically, the $[Cl^-]/[OH^-]$ ratio increases due to combined chloride accumulation and decreased pH

within the crevice. Therefore, as-received rebars with rust layers and/or mill scale are generally more susceptible to corrosion initiation than polished rebar [3–6, 13].

In addition, Fe(III)-rich phases in rust layers may catalyse anodic activity by increasing the area of cathodic surfaces and forming galvanic couples, especially under wetting/drying conditions. However, there is some controversy about whether oxygen reduction can take place on a mill scale because of its semi-conductive nature [5]. When concrete is partially dry, oxygen reduction is limited due to an increase in



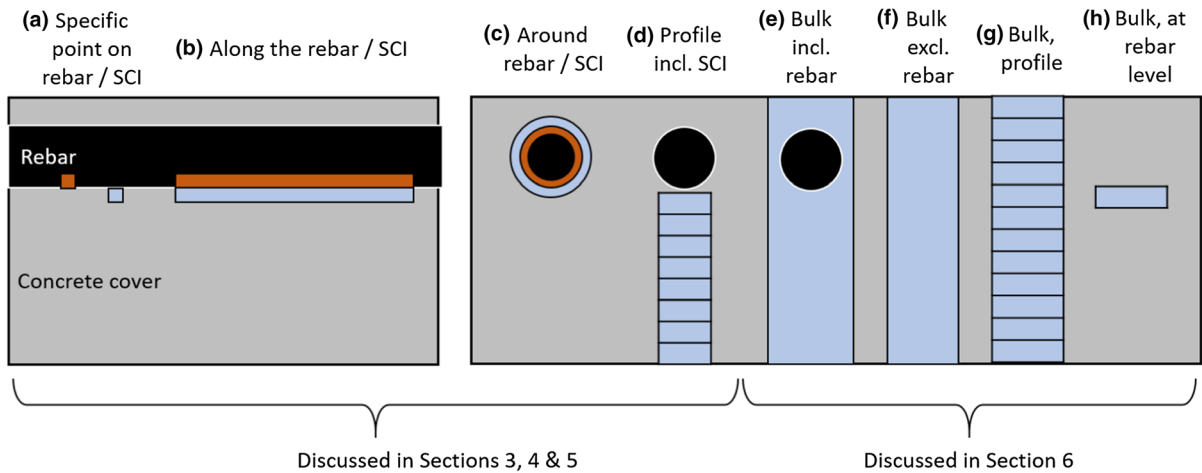
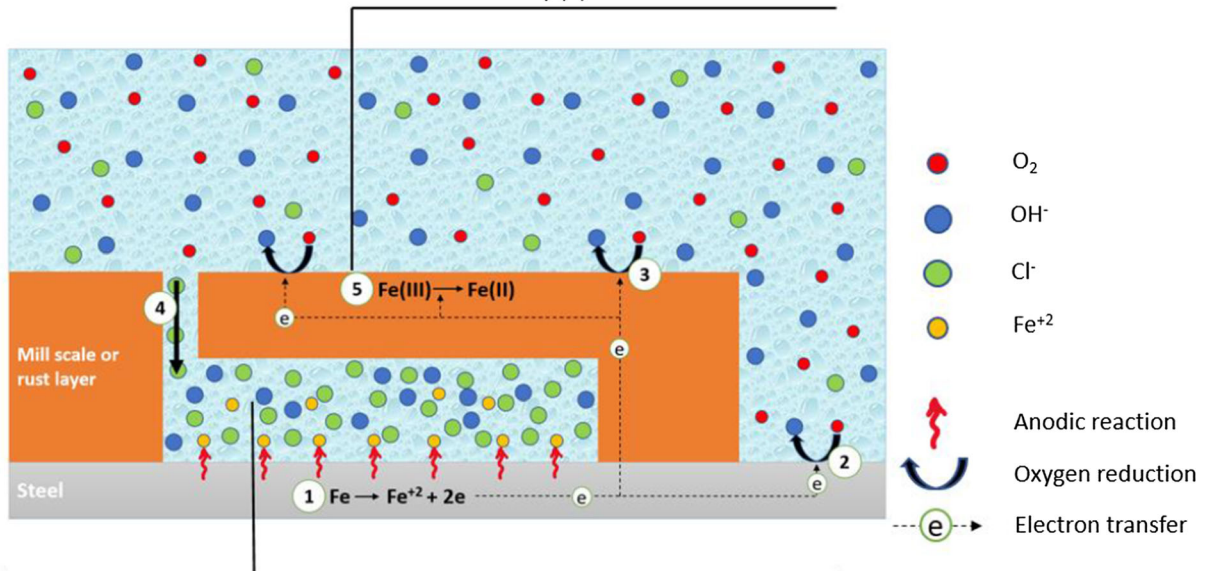


Fig. 1 Location and scale of measurements (left: longitudinal; right: cross-section). The orange and blue zones represent measurements performed at the steel surface and in the concrete, respectively

On mill scale / rust layers:

Fe(III)-rich phases allow oxygen reduction on mill scale / rust layers (5), which can catalyse the anodic activity (1)



Within crevice:

- Anodic reaction (iron dissolution) on the steel surface (1)
- Cathodic reaction (oxygen reduction) stops due to oxygen depletion, but it can take place on mill-scale free steel surfaces (2) or on mill scale/rust layers (3)
- Increased chloride ingress into the crevice (4) through crack/opening to bulk solution
- $[Cl^-]/[OH^-]$ becomes larger than that of outside crevice

Fig. 2 Increase in $[Cl^-]/[OH^-]$ and decrease in pH within a hypothetical mill scale crevice [13] and reduction of Fe(III)-rich phases to Fe(II)-rich phases on mill scale/rust layers [5]

Fe(III)-rich phases (which are generally insulating) and the lack of an electrolyte needed for the electrochemical reactions to occur at an appreciable rate [14]. When concrete is saturated, the Fe(III)-rich phases can be reduced to Fe(II) compounds, and this generates a cathodic current (in addition to the oxygen reduction reaction) to sustain anodic reactions [14, 15] in the crevice. As a result, the presence of rust layers (and potentially mill scale) may have a catalysing effect on the corrosion process, as illustrated in Fig. 2.

Due to the importance of mill scale and rust layers to corrosion, it is critical to characterise their morphology/geometry, composition and mechanical properties. Several methods to achieve this are reviewed below.

3.2 Morphology and chemical characterisation

3.2.1 Optical microscopy

Optical microscopy via stereo or compound microscopes can be used to characterise the morphology (i.e., thickness, pattern, and distribution) of mill scale and rust layers on the steel surface in a relatively fast and cost-effective manner. The technique can be used on rebar as received from the mill [12, 16], after mechanical separation from mortar/concrete [17], or as part of a general investigation of SCI on sectioned samples [16, 18]. Optical microscopy can also visualise corrosion products that form and their penetration into pores and cracks in the surrounding concrete [19].

A stereo microscope provides a low magnification overview of the mill scale and rust layers. Although the useable magnification is typically limited to $\sim 50\times$, it is simple to operate and does not require

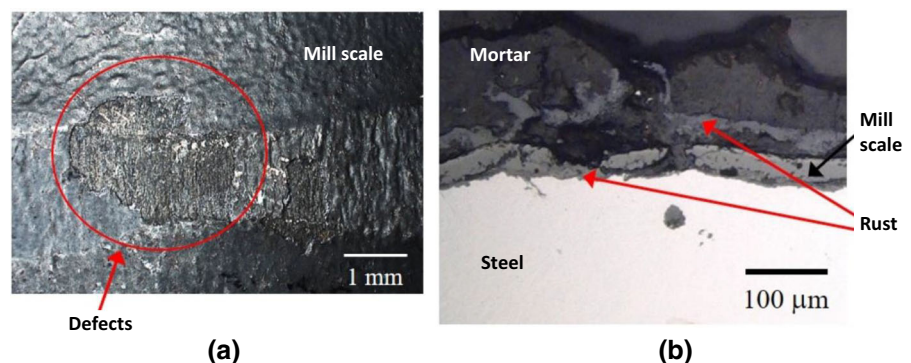
extensive surface preparation. The large working distance and depth of field allow three-dimensional visualisation of texture, roughness, crack opening, etc. For example, Fig. 3a shows the texture of the mill scale that highlights the discontinuity and defects along the rebar.

With a compound microscope, higher magnifications can be achieved, but this requires sample preparation to obtain a flat ground and finely polished surface. Figure 3b illustrates the application of high-resolution optical microscopy to characterise the morphology of mill scale and rust layers on a polished reinforced mortar specimen that has been exposed to chlorides. It shows rust forming at micron-sized defects between the mill scale and steel substrate, in line with the crevice corrosion mechanism presented in Fig. 2.

Resolution can be defined by the Abbe diffraction limit and Rayleigh criterion, as a function of the illumination wavelength and numerical aperture of the objective lens. On this basis, the theoretical resolution limit for optical microscopy is ~ 0.2 micron. In practice however, the achievable resolution is further degraded by other factors related to microscope optics, illumination, specimen surface quality, feature contrast, pixel size and segmentation accuracy.

Sample preparation for microscopy is a highly skilled and specialised activity but critical for obtaining good reliable data with minimal artefacts [20]. Although optical microscopy on etched surfaces can show microstructural details (e.g., to identify ferrite, pearlite and austenite grains) [17, 21], it does not provide information on chemical composition. Therefore, optical microscopy is usually complemented with other techniques such as scanning electron

Fig. 3 Optical micrographs showing **a** mill scale discontinuity on rebar surface, and **b** morphology of mill scale and rust layers on a cross-section of reinforced mortar subjected to chloride-induced corrosion [16]



microscopy (SEM) coupled with energy dispersive X-ray (EDX) spectroscopy or Raman spectroscopy.

3.2.2 Scanning electron microscopy (SEM)

SEM allows high-resolution characterisation beyond the capacity of optical microscopy. It is usually operated in the secondary electron (SE) or the backscattered electron (BSE) mode. The SE mode uses low-energy elastically scattered electrons to give morphological and topographic information at nanoscale resolution. The BSE mode is particularly useful because it allows differentiation between mill scale, rust layers and other phases [12, 16–19, 22] based on their atomic contrast and brightness intensity (see also Sect. 4.2.2). Furthermore, the elemental composition can be obtained when BSE is coupled with EDX spot analysis, line scan or mapping.

For example, Fig. 4a, b presents SEM-BSE micrographs of as-received rebar cross-sections that show the presence of pores, cracks, and crevices in the mill scale [12]. The mill scale has a variable thickness, coverage, and composition. EDX analyses indicate

differences in Fe/O ratio within the brighter inner layer (probably wüstite) and darker outer layer (probably magnetite), consistent with findings from Raman spectroscopy (see Sect. 3.2.3). Figure 4c, d shows an example SEM-BSE-EDX characterisation of the SCI subjected to chloride-induced corrosion [22]. The mill scale shows deterioration, and rust can be seen forming at the interface between mill scale and steel. EDX shows a higher concentration of Cl in this region consistent with the mechanism described in Fig. 2 and penetration of corrosion products into the adjacent porous cement paste matrix. Quantitative methods for determining the chloride concentration via EDX have been reported elsewhere [23].

Preparation of metallic samples for SEM is relatively straightforward but includes polishing or etching depending on the goal of the study. Samples that contain SCI require additional preparation such as impregnation with low viscosity epoxy, sectioning, SiC grinding, diamond polishing and coating with a thin conductive layer to avoid charging artefacts for high-vacuum imaging [24]. Carbon is typically used as the conductive coating to avoid interference with Cl

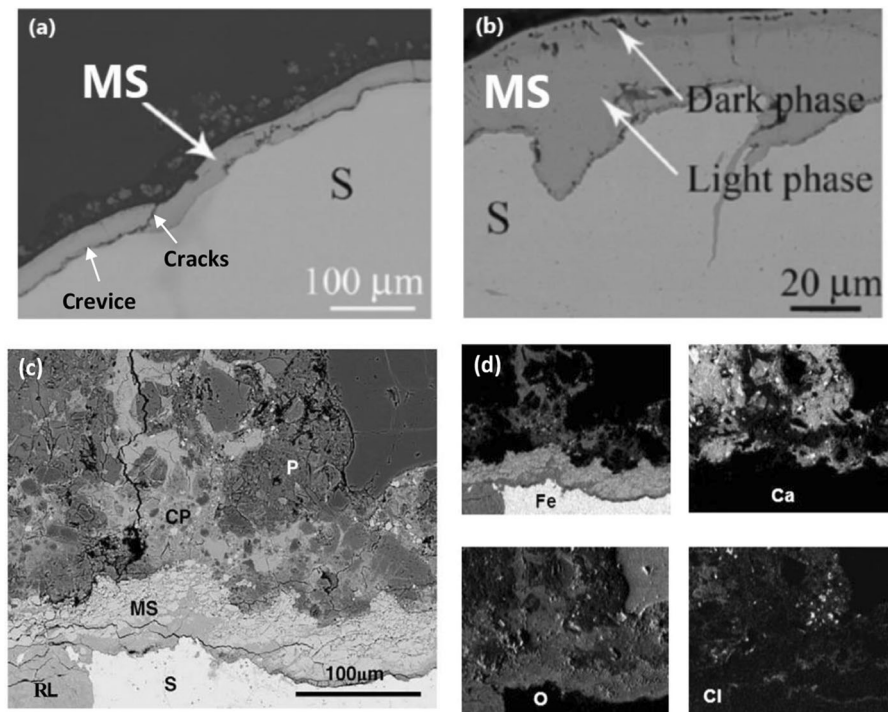


Fig. 4 a, b SEM-BSE micrographs showing mill scale on as-received rebar [12]; c SEM-BSE micrograph showing rust layers, mill scale, and chloride-induced corrosion products

penetrating the cement paste; d EDX mapping of Fe, Ca, O, and Cl. (S: steel; MS: mill scale; RL: rust layer; CP: corrosion products filled paste; P: paste) [22]

and other elements. Extracting these sub-samples from a larger specimen can cause damage; however, procedures are available to minimise these issues [25].

Electron backscatter diffraction (EBSD) is another promising SEM-based technique that can be used to determine the crystallographic structure of metal oxides [26] and provide insights into phases that have similar compositions. However, we are not aware of any substantial EBSD studies applied to the SCI to date, presumably due to difficulties in achieving the high level of surface quality required.

3.2.3 Raman spectroscopy

Raman spectroscopy is a chemical analysis method based on the characteristic energy shift known as Raman scatter, produced from the interaction between a monochromatic laser with the chemical bonds within a material. The technique can be used as point analysis or spectral mapping to give images at micron-scale spatial resolution. The Raman spectrum provides chemical and structural information, and phases can be identified by comparison with reference spectra of pure phases.

Raman spectroscopy has been used to characterise iron oxides and oxyhydroxides, including mill scale, rust layers, and corrosion products at the SCI [27–34]. However, attempts to study passive film were unsuccessful because it was too thin to be observable [29]. Section 3.2.4 provides some guidance on nano-scale surface characterisation techniques. The majority of these studies indicate that mill scale is primarily composed of wüstite (FeO) and magnetite (Fe₃O₄), with a surface layer of hematite (α -Fe₂O₃) and goethite (α -FeOOH) [27, 28, 33]. In the presence of chloride, the main corrosion products are mixtures of poorly crystalline iron oxyhydroxides, goethite (α -FeOOH), lepidocrocite (γ -FeOOH), akaganeite (β -FeOOH) and maghemite (γ -Fe₂O₃) [30, 31, 34].

Steel specimens can be analysed without surface preparation, but intact SCI would require preparation in the form of epoxy mounting, SiC grinding, and diamond polishing [32–34]. Some iron compounds are susceptible to thermal degradation from laser irradiation [35]. Therefore, the laser power must be filtered to less than 0.1 mW to avoid thermal effects [30, 34]. Furthermore, the Raman shifts of many iron

compounds are either close or overlapping, and are challenging to discriminate, particularly in mixtures within the analysed volume [32, 34, 36, 37]. The Raman spectra and main peak positions of major iron compounds can be found in the preceding references.

3.2.4 Nano-scale surface characterisation

The techniques described previously are appropriate for micrometre-scale features. For nano-scale passive film and native oxide films, other methods such as X-ray photoelectron spectroscopy (XPS) and transmission electron microscopy (TEM) are required [38–41]. XPS can identify all elements (except H and He) and their chemical state within a surface depth of ~ 10 nm. Samples may require polishing to reduce topographic variability. XPS can also provide the oxidation state of iron species in the analysed depth [38, 39, 42]. The technique is non-destructive when used in the angle-resolved mode but could change oxidation states if used as a depth-profiling tool for elemental composition.

TEM requires electron transparent thin sections (typically ~ 100 nm thick) extracted using focused ion beam (FIB) milling. The samples can also be used with EDX to obtain elemental information and electron energy loss spectroscopy (EELS) to provide information on the atomic composition, chemical bonding, valence and conduction band electronic properties, surface properties, and element-specific pair distance distribution functions [41]. However, it should be noted that these nano-scale techniques are not commonly used for characterising the SCI.

3.3 Micromechanical properties

Micro/nano-indentation is a depth-sensing technique for determining mechanical properties such as Young's modulus and hardness within a local volume of material. It works by pressing a small tip (indenter) of known geometry and mechanical properties into the sample at increasing load, and subsequently analysing the load versus displacement data [43]. The method requires flat-polished samples prepared similarly to SEM-BSE (Sect. 3.2.2) and has been applied to characterise mill scale and corrosion products [33, 44–47].



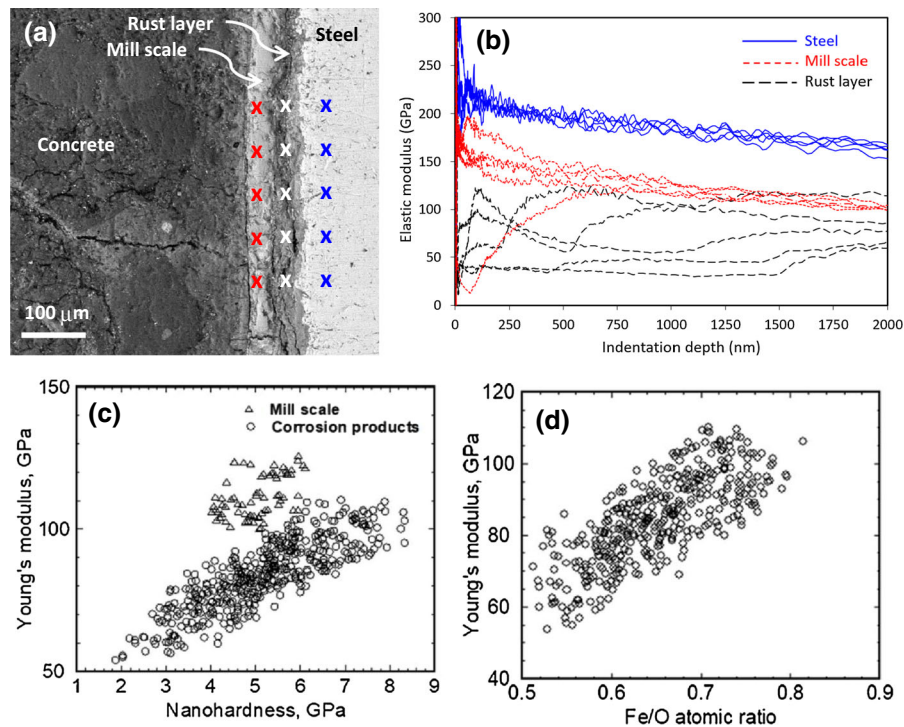


Fig. 5 a, b SEM-BSE micrograph indicating nano-indentation locations on corroded SCI and the variation in measured elastic moduli with indentation depth [44]. c, d Correlations between

Young's modulus, nano-hardness and Fe/O atomic ratio (EDX) for mill scale and corrosion products at the SCI showing large scatter [33]

An example application of nano-indentation on SCI subjected to chloride-induced corrosion is shown in Fig. 5a, b [44]. It can be seen that the measured elastic moduli fluctuate with indentation depth and stabilise at $\sim 2 \mu\text{m}$. Nevertheless, the obtained averages are distinct for steel ($\sim 183 \text{ GPa}$), mill scale ($\sim 122 \text{ GPa}$) and rust layer ($\sim 47 \text{ GPa}$). The latter shows a high degree of scatter, suggesting variable composition and mechanical properties. These trends are consistent with data from other studies [33, 45–47].

Figure 5c, d shows positive correlations between Young's modulus, hardness and Fe/O atomic ratio (from parallel EDX analyses), obtained from > 500 indentations of mill scale and corrosion products at the SCI [33]. The results suggest that micromechanical properties of corrosion products increase with Fe/O atomic ratio, but large scatter occurs locally due to the complex mixture of phases within the rust layer, consistent with findings from Raman spectroscopy (Sect. 3.2.3). The ability to resolve these complex mixtures is challenging and not yet achievable with current instrumental capabilities.

4 Interfacial voids and concrete microstructure

4.1 Background

Macroscopic interfacial voids play an important role in chloride-induced corrosion initiation [2]. These include entrapped or entrained air adjacent to the steel, settlement and bleeding zones, and mechanical damage such as cracks, slip and separation [1]. Additionally, microstructural features such as the paste porosity [48] or phase assemblage [49] and their gradients from the steel surface are important for corrosion processes. It is thus critical to be able to study and quantify these characteristics.

A pertinent issue is the role of macroscopic interfacial voids. Various studies have attempted to address this issue, however, with contradictory conclusions [2]. A general limitation of many studies was that the methods used did not allow for an accurate determination of the exact location of corrosion initiation concerning the location of interfacial voids. As schematically shown in Fig. 6, localised corrosion may, in some cases, start close to a void but later

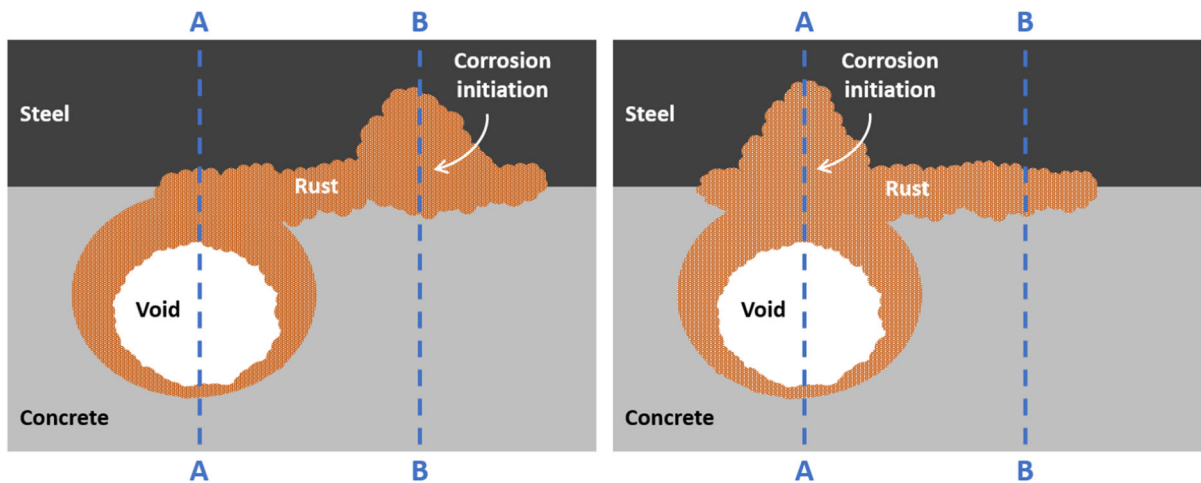


Fig. 6 Schematics showing possible locations of corrosion initiation relative to interfacial voids. Dashed lines (A, B) represent possible sections investigated in two-dimensional characterisation methods and the related misinterpretation risk

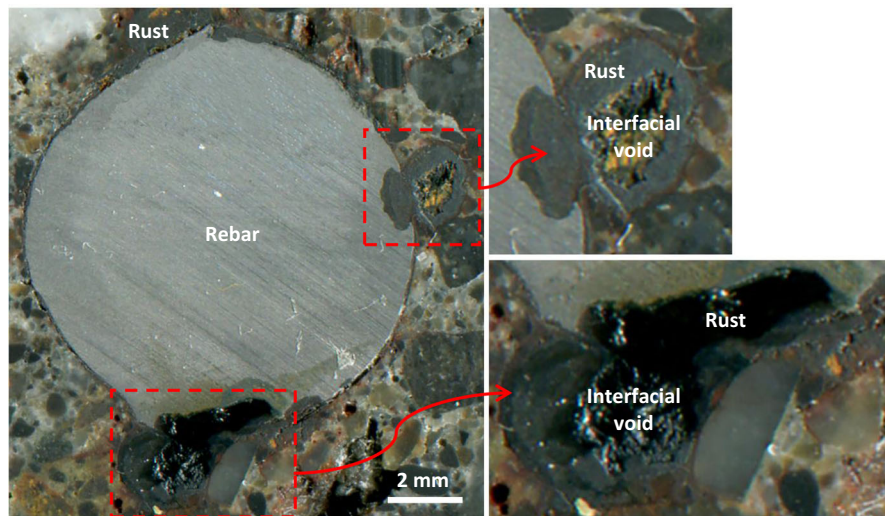


Fig. 7 Optical microscopy image showing macroscopic interfacial voids filled with corrosion products [54]

spread towards it and cause corrosion products to precipitate within the void. In other cases, corrosion may initiate at the void and later spread to other areas where the environment is more favourable for corrosion. Figure 7 illustrates that the location of studying these phenomena, namely through 2D cut sections (see Sect. 4.2), bears a risk for misinterpretation of the results.

It is also important to distinguish whether an interfacial void is directly in contact with the steel or separated by a thin cement paste layer, which provides a pH buffer against corrosion initiation. Yet, this may

not be readily apparent because precipitated corrosion products could mask the cement paste at the SCI (Figs. 7 and 8). Furthermore, the paste may be damaged in experiments where rebar is physically removed to observe the imprinted SCI, which is a common practice. Another complicating factor is that the moisture state of interfacial voids largely influences its susceptibility to corrosion initiation (Sect. 5.1). These scenarios have different implications for the corrosion initiation mechanism, and thus reliable documentation is needed to obtain fundamental understanding [2].

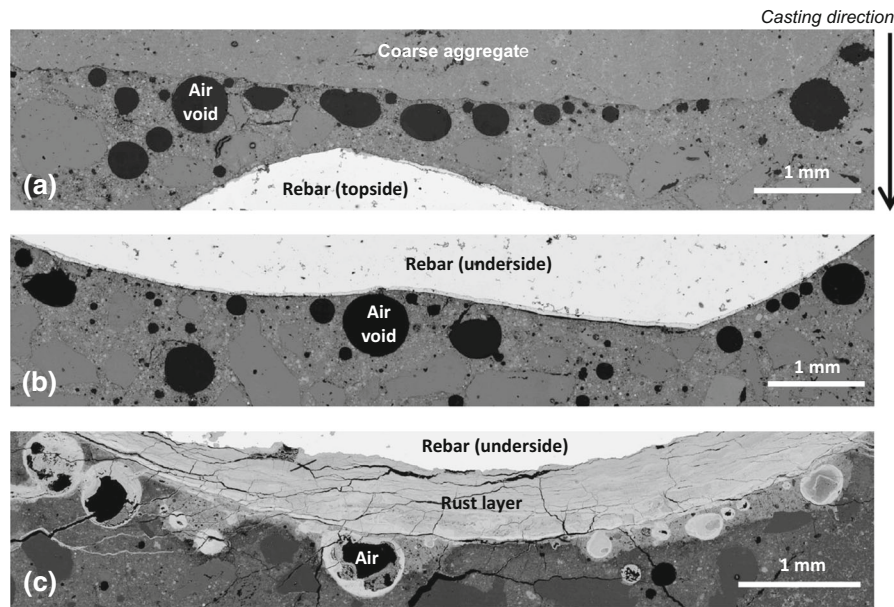


Fig. 8 BSE montages showing **a** entrapped air voids beneath a coarse aggregate particle near a rebar; **b** entrapped air voids beneath a rebar; and **c** severely corroded specimen showing accumulation of corrosion products at the SCI and penetration

into cement paste, air voids and cracks [22]. Note that the air voids are nearly spherical and that only the tips are in contact with the rebar (courtesy of Hong Wong, Imperial College London, UK)

Such considerations define the information required to prove hypotheses related to the effect of interfacial voids and microstructure at the SCI. For example, characterisation methods need to deliver quantitative information on the size/length, shape, and distribution of voids, particularly their location with respect to corrosion initiation spots. For these investigations, the spatial resolution needs to be in the micron range. Furthermore, microstructural features such as cement paste porosity, phase assemblage, corrosion products and their spatial distribution within the SCI must be characterised, ideally at submicron resolution.

4.2 Two-dimensional characterisation

A common approach is to prepare sections perpendicular to the steel and view them with optical microscopy or SEM (e.g., sections A and B as schematically illustrated in Fig. 7). These two-dimensional microscopy techniques can reliably distinguish different phases at a high resolution. They can also be combined with other techniques (e.g., EDX, Raman spectroscopy) to yield further insights on phase composition. Another approach is to split the

specimen, carefully remove the rebar, and observe the SCI imprint. This allows the examination of voids and corrosion spots over a wider interfacial area along the rebar.

The main disadvantage is the destructive nature of the sample preparation, which requires cutting, drying, evacuation, resin impregnation, and several mechanical grinding and polishing stages. These are delicate, time-consuming and costly processes that are prone to induce artefacts or damages [24, 25]. Thus, appropriate equipment, technique and expertise are required to produce reliable data. This approach can only probe the microstructure at a particular point in time, and continuous monitoring is not possible.

Furthermore, precipitates may mask certain interfacial features, and correct interpretation may be difficult due to the lack of three-dimensional information. It is also not possible to characterise the amount or the chemistry of the aqueous solution at the SCI since samples are dried. Representative sampling is challenging for techniques that require rebar removal, particularly where a thin cement paste separates voids from the rebar, or where the microstructure is already weakened by corrosion.

4.2.1 Optical microscopy

Optical microscopy has been used in numerous studies to characterise interfacial voids and concrete microstructure. The imaging is usually carried out in reflected mode using visible or UV light (to induce fluorescence). It is rarely possible to characterise SCI using transmitted or polarised light because of difficulties with preparing thin sections containing rebar [50]. The main application is the study of macroscopic features such as rebar, mill scale (Sect. 3.2.1), interfacial voids, bleed water zones, cracks and corrosion products [51–53]. These features are distinguished solely from their colour, shape and location, and the characterisation is qualitative unless images are captured, digitised and measured with image analysis. For polished cementitious materials in reflected light, the smallest resolvable feature is likely to be several microns (see Sect. 3.2.1).

Figure 7 shows an example of optical microscopy applied to visualise the distribution of interfacial voids and corrosion products at the SCI. The specimen was subjected to corrosion in a cyclic wetting/drying natural marine environment, then sectioned and flat ground with SiC, and imaged using a stereomicroscope. The observation suggests a spatial correlation between corrosion spots and macroscopic voids at SCI. However, it is difficult to draw any definitive conclusion on the exact location of corrosion initiation due to the uncertainties discussed earlier (Fig. 6).

4.2.2 Scanning electron microscopy

SEM has been used in many studies to characterise the microstructure of SCI. Earlier studies have focussed on detecting calcium hydroxide and corrosion products [55–59] using secondary electron (SE) imaging. This imaging mode is well suited for studying morphology and orientation. However, it is carried out on fractured surfaces, which could be damaged and therefore misleading. Furthermore, it is challenging to obtain compositional information, quantitative data or meaningful comparison between samples.

A more objective and informative approach is the backscattered electron (BSE) mode on epoxy impregnated polished sections [60]. This allows high-resolution characterisation of air voids, capillary pores, cracks, unreacted cement, hydration products, aggregates, mill-scale and corrosion products (Sect. 3.2.2)

based on brightness intensity (Fig. 8). Furthermore, quantitative information can be extracted via stereology and image analysis. For example, the amount, size and spatial distribution of various phases at the SCI can be obtained at pixel resolution [61, 62].

The achievable spatial resolution is dependent on the electron-solid interaction volume, phase contrast and other factors such as the electron source (emitter type), detector efficiency, sample preparation quality and image segmentation. A sub-micron resolution can be achieved for epoxy-filled voids depending on the SEM type and image segmentation [63, 64]. Another advantage of SEM-BSE imaging is that it can be combined with EDX [34, 65, 66], Raman spectroscopy (Sect. 3.2.3) and nano-indentation (Sect. 3.3) to obtain chemical and micromechanical properties. However, it requires extensive sample preparation (Sect. 3.2.2) that may induce changes to the SCI.

4.3 Three-dimensional characterisation

To overcome the limitations of two-dimensional characterisation discussed above, approaches utilizing non-destructive radiation (X-ray, neutrons) or destructive layer-by-layer milling and imaging have been used. The advantage of non-destructive techniques is that they allow continuous in-situ monitoring of corrosion processes. The drawbacks are generally lower spatial resolution and larger uncertainties in phase identification. While radiographic techniques provide some three-dimensional information from integral attenuation, only tomographic techniques allow complete 3D reconstruction. Besides providing visual observation, computed tomography entails the possibility of developing 3D models for simulation of, for instance, microstructure, mechanics and mass transfer.

4.3.1 X-ray imaging

X-ray micro-computed tomography (μ CT) has gained significant attention for characterising three-dimensional voids, pores and microcracks in hardened cementitious materials [67–70] due to its non-destructive nature and ease of sample preparation. The achievable spatial resolution is around one-thousandth of the specimen diameter [71]; therefore, small specimens are required to obtain high spatial resolution. State-of-the-art laboratory μ CT can provide



micrometre scale resolution for specimens of a few mm in diameter, while synchrotron sources can achieve better resolution, but are rarely used due to limited access. Nanotomography may yield information down to the sub-micrometre scale [72].

However, there are challenges and limitations when applying X-ray imaging to SCI. Obtaining small specimens from the SCI (as opposed to bulk cement paste/mortar) in an undisturbed state to achieve micrometre scale resolution is extremely difficult. This is due to challenges associated with cutting or drilling small specimens covering the SCI from larger specimens [25]. Thus, X-ray imaging of the SCI is typically limited to a resolution of tens of micrometres. Another challenge relates to the large mismatch in X-ray photoelectric absorption between steel and concrete, causing low feature contrast in the latter. Furthermore, the presence of steel induces beam hardening artefacts (for polychromatic X-ray sources) that distort the imaged SCI [25, 45, 73–75].

These artefacts hamper reconstruction and correct segmentation of the SCI, especially for realistic rebar geometries, which render accurate analysis difficult. Some of the artefacts may be reduced by using small hollow cylindrical rebar and filtering or post-acquisition data processing, at least for simple geometries (smooth/plain) in well-controlled laboratory conditions [76–78], or by using synchrotron X-ray sources. For simple rebar geometries, μ CT can be used to study certain microstructural SCI features, such as cracks (Fig. 9), interfacial voids, corrosion pits and corrosion-induced damage [45, 79–84].

4.3.2 Neutron imaging

Neutron imaging is based on measuring the intensity of a transmitted neutron beam through an object, either in two-dimension (radiography) or three-dimension (tomography) [85]. It is similar to X-ray imaging in the sense that it allows non-destructive characterisation with almost no sample preparation required. However, neutron imaging is less commonly used due to limited availability of beamline facilities. Typical setups can achieve a field of view of 40×40 cm ($200 \mu\text{m}/\text{pixel}$) to 0.5×0.5 cm ($5 \mu\text{m}/\text{pixel}$). Its resolution improves with small specimens and is considered to be about $10\text{--}20 \mu\text{m}$ for the smallest achievable field of view [86, 87]. The main advantage of neutron imaging over X-ray imaging is the absence of steel artefacts as discussed in the previous section. This is because neutrons are almost completely transparent to steel, but strongly attenuated by hydrogen-rich phases such as the moisture (see Sect. 5.3.2), hydrated cement paste and corrosion products. Figure 10 shows an example that highlights the feasibility of this technique when applied to reinforced concrete.

Neutron tomography has been used in a few exploratory studies to visualise the spatial distribution of voids, aggregate particles, cracks and corrosion products at the SCI [88–90]. For example, Garbe et al. [89] observed large voids ($\sim 50 \text{mm}^3$) adjacent to reinforcement steel at the SCI. Zhang et al. [90] used neutron tomography to visualise the spatial distribution of corrosion products in mortar reinforced with an 8 mm rebar subjected to load-induced damage and

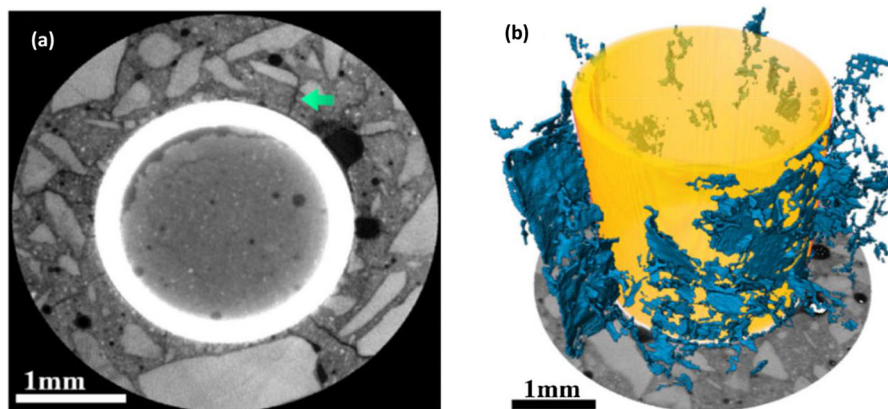


Fig. 9 **a** X-ray μ CT slice showing cracks and voids at the interface between mortar and cylindrical steel tube; **b** 3D rendering of the segmented cracks (blue) and steel tube (yellow) [25]. (Color figure online)

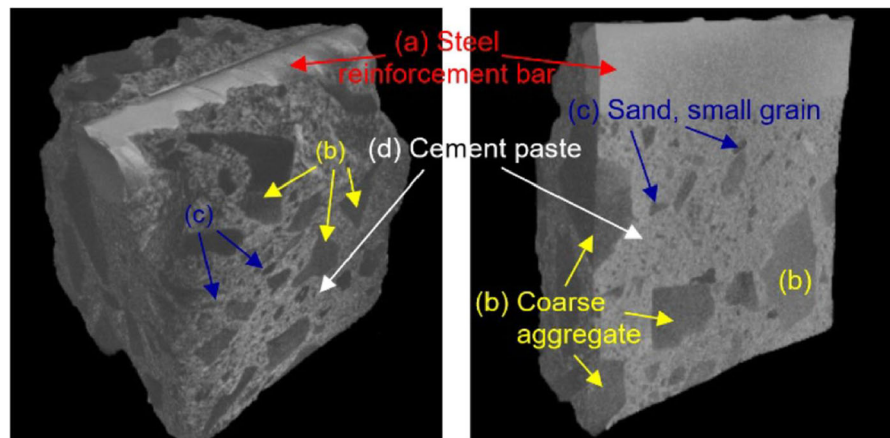


Fig. 10 Neutron tomography of a reinforced concrete showing the cement paste and spatial distribution of aggregate particles around ribbed steel reinforcement [88]

wet/dry cycles of 5% NaCl solution. They observed corrosion products mainly at the location of cracks (60–120 μm width). However, the pixel dimension used in these studies was relatively coarse (55–59 μm). Nevertheless, we believe that neutron tomography has considerable potential to be developed further for characterising the SCI non-destructively.

4.3.3 Bi-modal X-ray and neutron imaging

Combining X-ray with neutron imaging could be advantageous because of their complementary attenuation characteristics in reinforced concrete. For instance, Garcez et al. [88] used this combined approach to visualise three-dimensional flaws in structural concrete. X-ray imaging allows reliable segmentation of the rebar, while neutron imaging can be used for segmenting concrete microstructural features and corrosion products. Furthermore, complex data fusion and bimodal segmentation can distinguish features with similar contrast in one imaging mode but different contrast in the complementary mode. This approach was used in the recent research conducted by Boschmann [91] to study corrosion products and voids (Fig. 11). Cylindrical specimens (25 mm) with a centrally embedded rebar (diameter 10 mm), taken from existing engineering structures and later subjected to chloride-exposure conditions to trigger corrosion initiation in the laboratory, were imaged by X-ray and neutron tomography. With these specimen dimensions, the smallest

detectable air void (empty or filled with water) was $\sim 50 \mu\text{m}$. Figure 11 shows an example of a section from the tomographic data with segmented phases, namely cementitious matrix, steel, voids, and corrosion products. More recently, Robuschi et al. [92] used bimodal X-ray and neutron imaging to observe the SCI of naturally corroded reinforced concrete specimens containing 16 mm rebar. They were able to measure the volume loss of steel, iron-to-rust volumetric ratio, and the distribution of macroscopic interfacial voids and corrosion layer at a pixel size of $\sim 26\text{--}36 \mu\text{m}$.

4.3.4 Focused ion beam combined with scanning electron microscopy

Serial sectioning by focused ion beam (FIB) milling at nm precision followed by SEM imaging can be used to reconstruct 3D images of the microstructure. This method, known as FIB-nanotomography, has been used to study cementitious materials [93–95]. A significant advantage is that the milling is relatively gentle compared to mechanical cutting and grinding [96], which can induce artefacts at the SCI [25]. However, achieving representative sampling, although feasible, is a time-consuming process and quantitative analysis of the observed phases is complex [97]. For cement pastes, the representative elementary volume (REV) based on 3D pore structure characterisation is $\sim 100^3 \mu\text{m}^3$ [98]. Mortars and concretes are inherently more heterogeneous due to the presence of aggregates, interfaces and defects such as bleeding, segregation and microcracking. The REV

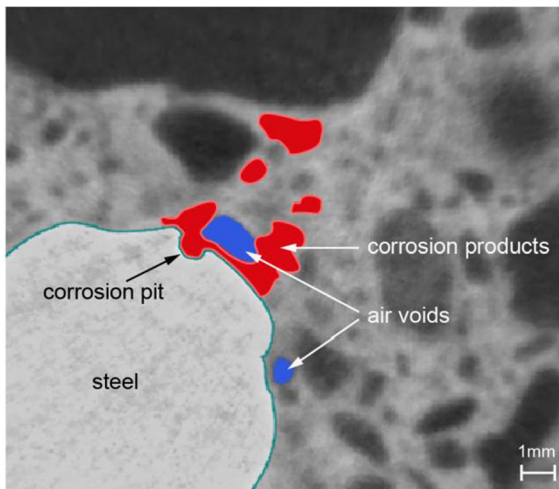


Fig. 11 Results of bimodal neutron and X-ray tomography [91]. Segmented cross-section showing air voids (blue) and corrosion products (red) at the steel–concrete interface

of these materials will be at least several times the largest aggregate particle size.

Figure 12 shows a preliminary application of FIB-SEM to study the interface between mortar and carbon-steel wire. The specimen was first carbonated to achieve corrosion initiation and then exposed to cyclic wetting/drying for several months [15]. Subsequently, it was sectioned across the steel wire and platinum-coated. A focused Ga^+ ion source (6.5 nA, 30 kV) was used to mill a trench to expose the internal steel-mortar interface for SEM-BSE imaging. The data reveals the steel, corrosion products, cementitious phases and pore space. The achievable resolution is similar to SEM-BSE, which is in the submicron range. This example illustrates the potential of FIB-SEM for characterising SCI, but clearly, more work is needed to establish the technique further.

5 Moisture content & spatial distribution

5.1 Background

The presence and movement of moisture have important direct impacts on the durability of concrete structures. Reviews by RILEM TC 262-SCI showed that moisture is a significant factor controlling the critical chloride threshold for corrosion initiation [2]. It was further hypothesised that in line with the

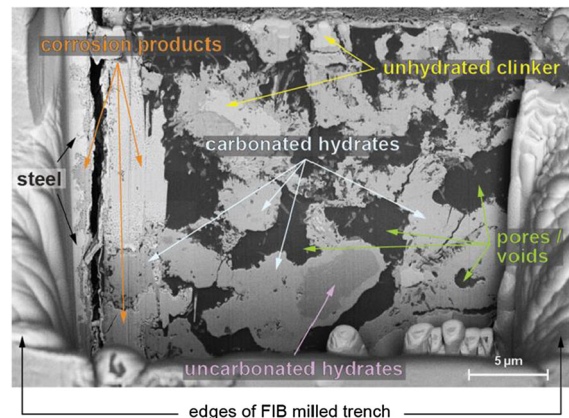


Fig. 12 Preliminary study using FIB-SEM on a steel-mortar interface (photograph: courtesy of Ueli Angst, Nicolas Ruffray and Zhidong Zhang, ETH Zurich, Switzerland)

mechanisms presented in Fig. 11 of reference [2], the moisture state of interfacial voids (Sect. 4.1) influences the susceptibility of steel to corrosion initiation and that this factor could explain the seemingly contradictory findings from different studies. However, the availability of moisture at the SCI is dependent not only on the exposure environment (wetting/drying, temperature) but also on a host of other factors including microstructure (e.g. capillary porosity and connectivity), presence of macroscopic interfacial voids and mechanical damage in the concrete cover [1, 2].

Macroscopic interfacial voids such as entrapped and entrained air voids, settlement and bleeding zones, cracks, slips and separations differ in length scale, geometry, initial moisture condition and access to the external exposure environment via the concrete cover [2]. All of these play a role in determining the long-term moisture state, availability of aggressive species and corrosion electrochemistry at the SCI. Unfortunately, these issues have received little research attention.

A recent overview of available techniques for determining the amount and state of moisture in building materials is given in [99]. Techniques that are suitable or potentially applicable to the SCI are reviewed here. These can be divided into absolute (e.g., gravimetry) or deductive methods, where moisture is determined by measuring a related property (e.g., electrical conductivity). To understand corrosion, we need the ability to detect the presence of moisture and determine its amount, state

(liquid/vapour, free/adsorbed/bound), chemical composition, and spatial distribution at the SCI, specifically within the voids, hydrates and corrosion products. However, none of the currently available techniques can achieve this.

5.2 Gravimetry

Determining moisture content in cementitious materials is commonly done by drying and measuring the associated mass loss. Gravimetry may also be used to obtain moisture profiles by analysing thin slices extracted at different depths [100]. The specimen size needed for such analyses depends on the accuracy and sensitivity of the balance and requirements for representativeness. This approach could be applied to the SCI if small specimens (~ 50 mg) are carefully extracted and subjected to thermogravimetric analysis (TGA) or dynamic vapour sorption (DVS). In TGA, the specimen is heated in steps of increasing temperature and weighed to determine the amount of free, adsorbed and chemically bound water. In DVS, the specimen is equilibrated to a range of vapour pressure at a constant temperature to determine water sorption isotherms. Both techniques use precise microbalance (resolution ~ 1 μg) and, as such, are highly sensitive.

A novel method to determine moisture state and content simultaneously via DVS is proposed here. In this approach, the specimen is transferred to the microbalance and the chamber RH is varied stepwise within an expected range. The specimen moisture state can be taken as equivalent to the chamber RH where it remains at or returns to its initial mass by monitoring asymptotic mass change. The number of iterations and step size will determine its accuracy; the latter should be kept small to reduce moisture hysteresis. The initial water content can subsequently be determined by drying to a well-defined state, e.g. 11% RH [101, 102].

These methods are potentially viable for characterising the SCI, but they will require further research and validation. The main challenges lie in extracting small representative specimens from the SCI and analysing them in an original undisturbed state. Accidental wetting/drying, carbonation or decomposition of volatile phases during sampling must be avoided. For TGA, the partial decomposition of C-S-H, ettringite and monosulfate at < 105 $^{\circ}\text{C}$ needs to be accounted for. For DVS, the issue of hysteresis needs careful consideration. In any case, the analysis of

moisture within macroscopic voids at the SCI is not possible at present with these techniques.

5.3 Radiation methods

5.3.1 X-ray imaging

X-ray imaging has been used to quantify relative changes (temporal and spatial) in water content of cementitious materials, rather than the actual absolute moisture content. A typical example is the study of waterfront movement during wetting [103] or drying [104] experiments using radiography (2D) and tomography (3D) techniques. Although radiography allows data acquisition at higher frequencies and thus achieve a better time resolution than tomographic measurements, the latter gives more information related to the three-dimensional transport process.

Typical challenges with these techniques concern detecting relatively small changes in density caused by water movement, the X-ray scattering artefacts caused by the heterogeneity of concrete and moisture distribution [105, 106], and measurement variability [107]. Contrast agents (e.g. CsCl) can be used to improve the signal-to-noise ratio [103], but this may affect the moisture transport phenomenon under study [105]. An alternative approach is phase-contrast imaging [105, 108]. Nevertheless, calibration is required, and common sources of error that affect resolution and accuracy include incorrect attenuation coefficients when calculating moisture content changes. Theoretical calculations indicate that X-ray imaging could observe changes in moisture content of approximately ± 1 kg/m^3 in concrete [106]. While actual measurements have not been able to achieve this level of accuracy, the method has been shown to detect the movement of moisture front from water ingress in conditioned (i.e. dried) concrete samples [107]. We are not aware of any studies that have successfully quantified moisture at realistic SCI geometries due to the limitations discussed in Sect. 4.3.1.

5.3.2 Neutron imaging

Neutron imaging is a promising non-destructive technique to study moisture content and movement in cementitious materials [85, 109–115]. This is because neutrons are strongly attenuated (absorbed and scattered) by hydrogen, producing a much higher



contrast between water-rich phases and other components compared to X-rays (see also Sect. 4.3.2). Neutron imaging may, under some conditions, detect changes of $\sim 1\%$ volumetric moisture content in cement-based materials [115]. The contrast may be further enhanced by using heavy water (D_2O) as a tracer in saturated samples since the neutron attenuation of deuterium is considerably lower than that of hydrogen.

Neutron radiography allows 2D projections to be acquired at intervals of a few seconds, while the acquisition of 3D tomographs is more time consuming, with measurement intervals of around 10 min [112]. Therefore, most studies on moisture transport have utilized radiography. Examples include quantitative measurements to determine the temporal and spatial variability of saturation degree in cementitious samples during water uptake [110–113, 115]. Brew et al. [110] detected macro-pores (volumes between 0.01 and 10 mm³) in paste and mortar samples. However, very few studies are related to moisture at the SCI. Zhang et al. [116] used neutron radiography to visualise the process of water penetration into a cracked steel-reinforced mortar. They observed rapid capillary absorption through the load-induced cover crack (0.35 mm width) and the steel-mortar interface that has been damaged presumably by the imposed flexural loading (Fig. 13).

As mentioned in Sect. 4.3.3, neutron tomography can be advantageously combined with X-ray imaging and this approach has been used to detect air voids (empty or water filled) down to $\sim 50 \mu\text{m}$ at the SCI [91]. We consider this a promising technique for future research, mainly because the presence of steel does not induce imaging artefacts, which is a limiting factor in

other methods such as X-ray (Sect. 4.3.1) and magnetic resonance techniques (Sect. 6.7).

6 Other methods

This section examines other methods that apply to the bulk concrete, steel or reinforced concrete, as a proxy to the SCI. These techniques cannot characterise the SCI directly due to the nature of the method itself, or the presence of a particular phase (e.g. steel) that severely complicates data analyses. However, these methods can provide averaged information relevant to the SCI, primarily when used under certain conditions or in combination with other methods.

6.1 Electrochemical techniques

Electrochemical techniques are widely used to study steel corrosion in concrete and can provide valuable data concerning the mechanisms associated with the presence of mill scale and rust layers on rebar surfaces [3, 7, 9, 79, 117–123]. Such techniques include but are not limited to, open-circuit corrosion (OCP) monitoring, linear polarization resistance (LPR), electrochemical impedance spectroscopy (EIS), cyclic voltammetry (CV) and coupled multi-electrode arrays (CMEA). However, they are not necessarily well-suited to characterise mill scale or rust layer as stand-alone techniques. The main limitation is that these techniques provide averaged data from the studied surface rather than localised properties and their spatial distribution.

Nevertheless, they can provide some relevant averaged properties of the mill scale and rust layers

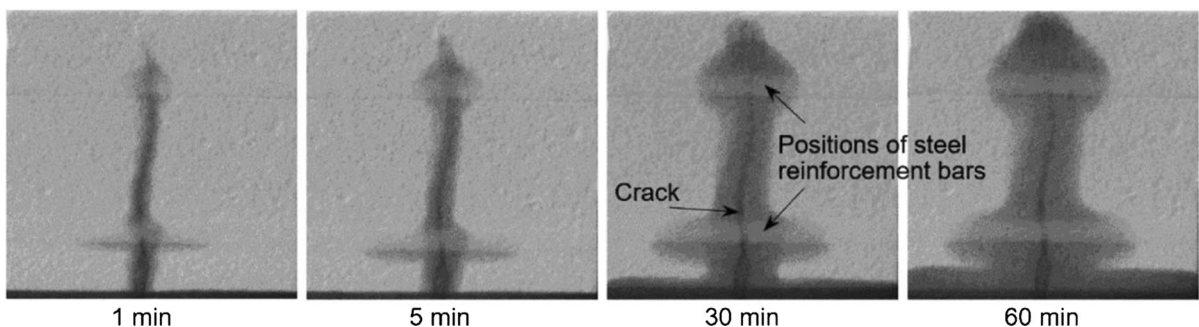


Fig. 13 Neutron imaging of water absorption into a reinforced mortar (8 mm rebar) from the bottom-exposed surface showing rapid ingress through a load-induced crack and the steel-mortar interface. Adapted from Zhang et al. [116]

when used as a tool to compare polished and as-received rebar in well designed-laboratory experiments. In particular, EIS can provide specific information about the average impedance of mill scale and rust layers, and other data such as their contributions to charge transfer resistance (R_{ct}), double layer capacitance (C_{dl}), etc. [124] when coupled with equivalent circuit modelling. Similarly, comparative CV experiments performed on polished and as-received rebar can provide information about the contribution of these layers to electrochemical oxidation/reduction reactions and characteristics such as pitting potential and re-passivating potential [125].

Local information about mill-scale and rust layer properties may be obtained through local electrochemical measurements, either by dedicated techniques applied to rebars [8, 126] or steel immersed in simulated solutions such as employing scanning vibrating electrode technique (SVET) or similar methods. CMEA has been used to measure local corrosion rates on rebar surface in mortar [79, 127] and shows promise in relating these measurements to heterogeneities in the SCI such as interfacial voids and moisture variations, when coupled with some of the other techniques described in this paper. To our knowledge, this has not been attempted before. Challenges related to the application of CMEA to study the SCI, particularly on the representativeness of CMEA with respect to rebar surfaces, are still to be tackled. A general advantage of many electrochemical techniques (e.g., OCP, LPR, EIS, CMEA, but for instance not CV) is that they are non-destructive; therefore, they can evaluate and capture changes of properties over time.

6.2 Mass transport based methods

Various researchers have used methods based on mass transport to visualise mechanical defects or bleed-water and settlement zones at the SCI that allow preferential mass transport. An example using neutron imaging to observe water ingress was described in Sect. 5.3.2. Another approach is based on exposing the reinforced concrete specimen to a chloride solution [128] or to CO_2 [129] for a specific time to allow these species to penetrate through cracks. Upon splitting the specimen, an indicator is applied, such as silver nitrate (for chloride) or phenolphthalein/thymolphthalein (for carbonation), to reveal the area along the SCI exposed

to chlorides or CO_2 , respectively. It is suggested that these areas correspond to damaged zones at the SCI, e.g. to settlement, slip and separation, which can be detected at μm scale resolution.

It should be noted that these methods rely on the existence of cracks to allow water, chlorides or CO_2 to access macroscopic voids at the SCI. In the absence of cracks, drilling a hole through the concrete cover to reach the SCI has been suggested. Nevertheless, a potential limitation of this approach is that it cannot reveal isolated voids at the SCI. Furthermore, the exposure and sampling may induce changes to the material (e.g. shrinkage cracking), and therefore the results must be interpreted with care to account for these factors.

6.3 Electrical resistivity

Electrical resistivity or conductivity has been suggested as a rapid non-destructive method to detect moisture ingress in concrete structures [130–132]. This is carried out using embedded sensors or Wenner-type arrays placed on the concrete surface. Multi-ring electrodes or comparable arrays are used to measure electrical resistivity as a function of depth and time, from which water profiles to the level of embedded steel and below could be estimated [131]. It is proposed that the local water content at the SCI could be estimated indirectly with appropriate calibration if the steel rebar is used as an electrode and other smaller electrodes are placed close to it. However, quantification of moisture in concrete is not straightforward because the measured electrical resistivity depends not only on the amount of moisture present but also on the pore structure, chemical composition of the pore solution, temperature and the presence of rebar or cracks. Furthermore, the embedded sensors will create additional interfaces and heterogeneities that could disturb the surrounding SCI microstructure.

6.4 Electrical resistance tomography

Electrical resistance tomography (ERT) is another method that allows non-destructive 3D visualization of moisture ingress and structural inhomogeneity (such as cracks, embedded rebar) in concrete from surface measurements [133–137]. The method is based on passing alternating currents through the specimen and measuring the resulting potential



differences using an array of surface-mounted electrodes. The internal distribution of conductivity is then mathematically reconstructed to form an image, from which moisture or other features may be contrasted. An extension of ERT is electrical impedance or capacitive tomography. The obtained conductivity can be converted to moisture content using experimentally-derived relationships, but this is a non-trivial task due to other influencing factors (e.g. pore structure, pore solution composition) as discussed in the preceding section. While ERT may yield information about moisture at the reinforcement depth (as a proxy for the SCI), it is challenging to obtain reliable data in the presence of embedded steel because the inversion of resistivity becomes increasingly complex. Furthermore, the spatial resolution of ERT is insufficient to provide void-scale or microstructural level information.

6.5 Infrared spectroscopy

Infrared (IR) spectroscopy is a technique for chemical analysis of solids, liquids or gases based on the vibrational energy of the chemical bonds present. A qualitative analysis (identification) of substances can be performed by referring to the position/shape of the absorption peaks in the IR spectrum, while quantitative analysis considers peak intensities and requires specific experimental calibration for the material investigated. Free water can be detected, for example, by the absorption bands at $\sim 3450\text{ cm}^{-1}$ and $\sim 1640\text{ cm}^{-1}$ that are due to the O–H stretching and H–O–H bending vibrations, respectively. Surface adsorbed and chemically bound water will show slight variations in the wave number due to hindered vibrations. While few available studies show that IR spectroscopy can detect changes in bulk moisture content [138], further research is required to establish its potential for characterising the local moisture state at the SCI.

6.6 Ground-penetrating radar

Ground-penetrating radar (GPR) is a non-destructive method based on the transmission of electromagnetic waves and analyses of the reflected signals from subsurface structures to detect changes in material properties. The characteristics of wave propagation are highly dependent on the dielectric properties of the

underlying medium, which in turn is moisture dependent. For example, the dielectric permittivity is 1 for air, ~ 81 for water and $\sim 4\text{--}10$ for concretes, dependent on the saturation degree [139, 140]. These characteristics support the use of GPR for evaluating moisture content in cementitious materials if the appropriate reference calibration exists [141, 142]. However, steel is an electromagnetic wave reflector and has an infinite dielectric constant. The presence of embedded steel rebars will significantly affect signals and the ability of GPR to characterise the SCI. Signal attenuation increases with an increase in sampling depth and saturation degree. Furthermore, its spatial resolution is of the order of several mm at best [143, 144], which may be sufficient to detect large voids in ideal situations. Comprehensive post-processing, calibration and interpretation will be required to understand radargrams, and we are not aware of any meaningful applications on characterising the SCI yet.

6.7 Nuclear magnetic resonance

Nuclear magnetic resonance (NMR) has been used to determine moisture profiles in a range of solid materials including concrete [145]. For quantitative analyses, the NMR signals are converted to water contents using the appropriate calibration curve for the actual concrete mix, determined from destructive gravimetric measurement. However, its spatial resolution is not considered sufficient to examine single voids in concrete. A significant complication is the presence of paramagnetic ions and the influence of steel rebar on the magnetic field. This requires correcting the electrical field using numerical methods, for example, based on the approach described in [146]. The use of single-sided NMR ex-situ on samples without reinforcement as a proxy will be more straightforward. NMR is also affected by similar limitations as those of other methods for characterising moisture at the SCI.

7 Discussion

7.1 Challenges and current limitations

Characterising the SCI is particularly challenging because of its physically and chemically complex nature that is multi-phase and multi-scale. Its



characteristics are spatially heterogeneous and time-dependent due to the many influencing factors, viz. processing, design, execution, hydration, mechanical loading, exposure conditions etc. Furthermore, steel and concrete display vastly contrasting properties. The SCI in actual structures is covered by a concrete layer, which itself is complex and heterogeneous. Furthermore, the SCI is fragile and prone to changes during sampling, preparation and characterisation. Laboratory studies of the SCI using relatively young, small-scale specimens or model systems in controlled exposure environments typically do not represent real structures. Indeed, our previous reviews [1, 2] have highlighted significant differences in the characteristics of SCI obtained from laboratory prepared specimens vs specimens retrieved from field structures.

Several factors need to be considered when selecting appropriate techniques for characterising the SCI. These factors include the achievable length scale (resolution, observation size), the property (physical/chemical) to be determined, whether or not a qualitative and/or quantitative assessment is needed, and what sensitivity, accuracy, and the spatial (lateral, depth) and temporal resolution are required. The ability to characterise the SCI in 3D is critical to avoid misinterpretation. Furthermore, it is essential to consider the requirements for sampling and sample preparation, the possibility of inducing non-reversible changes, and thereby preventing the ability to monitor time-dependent changes occurring at the SCI. Last but not least, the potential for field application of characterisation techniques on actual structures is essential, as discussed in the preceding paragraph.

Table 2 shows a summary of methods and their evaluation according to the criteria listed above. The information provided here complements Table 1, which summarises the features that can be characterised by each method, their location and scale. We recommend reading both tables together in order to gain a full appreciation of the state-of-art. It is clear that none of the available techniques satisfies every criterion or is sufficient on its own to provide the required information for a complete characterisation of the SCI. Thus, techniques need to be selected with care taking into account the scientific questions under study.

The review shows that there are good well-established options for direct characterisation of mill-scale, rust layer, concrete microstructure and interfacial

voids. The most viable and versatile quantitative methods are based on microscopy, e.g. optical imaging and SEM when combined with image analysis. However, all established methods require destructive sampling or preparation protocols that limit studies to single-point measurements in time. Thus, they cannot monitor microstructural changes or time-dependent processes, e.g. pit stabilisation and growth, and corrosion product formation. Nevertheless, several promising non-destructive techniques have emerged in recent years. More work is needed to fully establish and exploit these for characterising the SCI (see Sect. 7.2).

A common challenge for all imaging methods is obtaining representative samples of the governing features/processes at high spatial resolution. To illustrate this, Fig. 14 shows the field of view (FOV) plotted against spatial resolution for a range of techniques, based on published data relevant to the SCI. Here spatial resolution is calculated as $2.3 \times$ pixel size according to the Nyquist criterion, while FOV is taken as the largest image dimension reported in the respective study. It can be seen that resolution decreases with increasing image size and is larger than one-thousandth of the FOV for most methods. In theory, the FOV for OM, SEM and FIB-SEM can be extended indefinitely (by stitching consecutive images) without sacrificing resolution, but there are practical limits to this in terms of time, effort and cost. For X-ray and neutron imaging, there is an inevitable trade-off between resolution and image (specimen) size.

The achievable resolution and observation length scale shown in Fig. 14 mean that most studies are confined to small SCI regions that may not represent actual structures. Indeed, some SCI features important to corrosion do extend beyond this length scale [1, 2]. For example, cracks, slip and separation, settlement and bleeding zones can occur over several cm to m along the reinforcing steel bar, while having characteristic dimensions in microns. In actual structures, the macroscopic rebar geometry may influence corrosion initiation by modifying the SCI locally viz. ribs, intersections, and bent rebars. The length scale required for characterising these properties and their effects on corrosion remains an open question.

Currently, there are no proven techniques for characterising moisture characteristics at the SCI, for example, the amount, state (liquid/vapour) and spatial



Table 2 Summary of methods and their potential for characterising SCI

Method*	Length scale	Direct observation	Quantitative	Physical properties	Chemical properties	Three-dimensional	Non-destructive	Spatial & temporal	Field application
<i>Microscopy</i>									
Optical microscopy (OM)	µm-cm	✓	✓	✓	•	•	✗	✗	✗
Secondary elec. (SEM-SE)	nm-mm	✓	✗	✓	•	•	✗	✗	✗
Backscattered elec. (SEM-BSE)	µm-cm	✓	✓	✓	•	✗	✗	✗	✗
Focused ion beam (FIB-SEM)	µm	✓	✓	✓	•	✓	✗	✗	✗
Transmission elec. (TEM)	nm-µm	✓	✓	✓	•	•	✗	✗	✗
<i>Radiography and tomography</i>									
X-ray imaging (µCT)	µm-cm	✓	✓	✓	•	✓	✓	✓	✗
Neutron imaging	µm-cm	✓	✓	✓	•	✓	✓	✓	✗
Combined X and neutron imaging	µm-cm	✓	✓	✓	•	✓	✓	✓	✗
<i>Spectroscopy</i>									
Energy-dispersive X-ray (EDX)	µm-mm	✓	✓	✗	✓	✗	✗	✗	✗
Raman spectroscopy	µm-mm	✓	✓	✓	✓	✗	•	•	✗
X-ray photoelectron (XPS)	nm-µm	✓	✓	✗	✓	✗	✗	✗	✗
Infrared spectroscopy (IR)	µm-mm	✗	✓	•	✓	✗	✗	•	✗
<i>Physical</i>									
Nano/micro indentation	nm-µm	✓	✓	✓	✗	✗	✗	✗	✗
Thermogravimetric analysis (TGA)	mm	•	✓	✓	•	✗	✗	✗	✗
Dynamic vapour sorption (DVS)	mm	•	✓	✓	✗	✗	✗	✗	✗
<i>Others (less applicable)</i>									
Electrochemical	mm-cm	✗	✓	•	•	✗	✓	•	✓
Mass transport based	µm-cm	✗	•	✓	✗	✗	•	•	•
Electrical resistivity	mm-cm	✗	•	✓	✗	✗	•	•	✓
Elec. resistance tomography (ERT)	mm-cm	✗	•	✓	✗	•	✓	•	✓
Ground penetrating radar (GPR)	mm-cm	✗	•	✓	✗	•	✓	✓	✓
Nuclear magnetic res. (NMR)	mm-cm	✗	•	✓	✗	✗	✓	✓	✓

* Notes: We define a method as “indirect” if it applies only to the bulk concrete, steel or reinforced concrete, as a proxy to SCI (see Section 2 and Fig. 1). A method is “non-destructive” if it can characterise SCI in its native state without extensive sample preparation (e.g. sampling, cutting, drying, grinding, polishing etc.) that might alter the SCI characteristics. “Spatial & temporal” refers to the ability to capture changes in properties over space and time on a single specimen.



Table 2 continued

Symbols ✓ (yes) and × (no) indicate whether the method satisfies a particular criterion. Symbol • (maybe) indicates that the method partially meets the criterion under certain conditions

*We define a method as “indirect” if it applies only to the bulk concrete, steel or reinforced concrete, as a proxy to SCI (see Sect. 2 and Fig. 1). A method is “non-destructive” if it can characterise SCI in its native state without extensive sample preparation (e.g. sampling, cutting, drying, grinding, polishing etc.) that might alter the SCI characteristics. “Spatial & temporal” refers to the ability to capture changes in properties over space and time on a single specimen

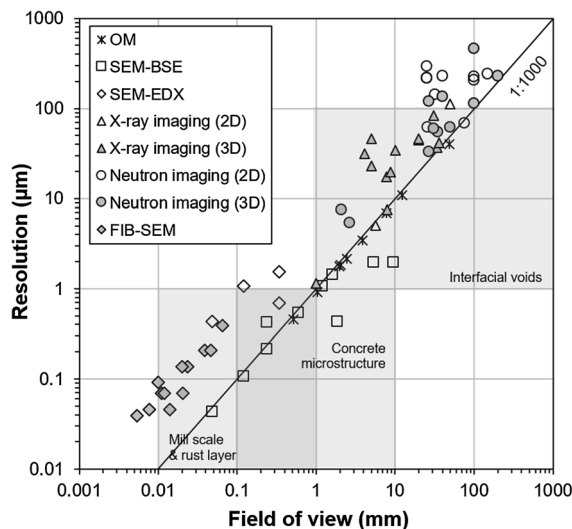


Fig. 14 Correlation between achievable spatial resolution (calculated from pixel size) and field of view for a range of imaging techniques reviewed in this study. Data compiled from [22, 25, 45, 62, 66, 67, 79–85, 92, 94, 95, 109, 110, 112–116]. Shaded boxes represent the relevant length scale for a particular feature of interest

distribution. Little is known regarding the degree of filling and adsorbed water film thickness in macroscopic interfacial voids. It is also not possible to characterise the chemical composition of the aqueous solution at the SCI. Another observation from Table 2 is the dearth of quantitative methods with good resolution suitable for characterising SCI in actual structures in the field. Available techniques can provide bulk averaged information only and lack well-documented evidence for studying the SCI due to various complications described previously.

7.2 Future opportunities and research needs

This review has shown great opportunities in pursuing and further developing the following characterisation techniques and approaches to enhance our understanding of the fundamental processes occurring at the SCI prior to, during, and after initiation of steel corrosion.

It is recognised by the authors that progress can be made in characterising mill scale and rust layers through advanced electrochemical and imaging methods. As discussed in Sect. 6.1, conventional electrochemical techniques provide averaged properties rather than localised information and spatial



distribution. However, other techniques less well-known in the cement and concrete community may overcome this limitation [8, 126]. These include scanning electrochemical microscopy (SECM), localised electrochemical impedance spectroscopy (LEIS) and scanning vibrating electrode technique (SVET). When coupled with optical microscopy, we believe that these techniques can provide valuable data on mill scale and rust layers to further our understanding of their role in corrosion processes. However, it should be noted that these electrochemical methods are carried out on metal surfaces immersed in simulated aqueous electrolytes, as opposed to the actual SCI.

To the best of our knowledge, X-ray μ CT has not been applied to characterise mill scale, cracks or pre-existing rust on ribbed/corrugated rebar. These features are below the spatial resolution that μ CT can offer for specimens of realistic dimensions, thereby rendering its use unviable. As such, future studies on small-scale model systems are needed to overcome this limitation. Other potential approaches to extend the capability of μ CT is integration with electrochemical measurements [147] and comparing experimental/theoretical linear attenuation coefficients to estimate the chemistry of the mill scale/corrosion products [83]. The latter relies on the theoretical densities of various iron oxides/hydroxides that may lead to discrepancies. This is compounded by the fact that these products are complex mixtures at the micron scale in a natural corroding system. Nevertheless, we see value in further exploring these approaches in future studies.

We believe that further advancement and application of 3D imaging is the way forward for characterising interfacial voids and concrete microstructure. For example, FIB-SEM tomography allows 3D characterisation at very high (sub-micron) pore-scale resolution. As discussed in Sect. 4.3.4, this technique can yield detailed information about the phase assemblage and microstructure of the cementitious phases at the SCI. Moreover, FIB-SEM tomography could potentially be used to study mill-scale and rust layers embedded in concrete. However, its destructive nature does not allow monitoring of processes and microstructural changes in-situ and over time. Nevertheless, strategic sampling and collection of 3D data in a statistical manner may enable the establishment of “digital twins” of the pore structure and solid phases present. Combining these data with numerical modelling at the pore scale, particularly ion and moisture

transport and chemical reactions of ferrous and other species within this interfacial zone [148–153], is expected to be instrumental in understanding processes relevant to corrosion at high spatial resolution.

A powerful technique for 3D non-destructive in-situ monitoring of local SCI features and processes related to corrosion, albeit at lower spatial resolution than FIB-SEM, is multimodal tomographic imaging, particularly bi-modal X-ray and neutron imaging. The major advantage of this as opposed to X-ray μ CT on its own is that the multimodal approach overcomes challenges related to the presence of the steel, as discussed in Sect. 4.3.1. Recent studies have shown that features such as macroscopic interfacial voids of various origins, local pitting corrosion, rust layer and precipitated corrosion products in the concrete matrix can be detected. Both spatial and temporal information are indispensable for gaining mechanistic insights into corrosion initiation and propagation, e.g., the role of interfacial air voids, and the transport and precipitation of corrosion products. Furthermore, neutron imaging techniques, both radiography and tomography, are considered highly promising for studying moisture distribution at the SCI. More work is urgently needed in this area.

Nuclear magnetic resonance (NMR), though not yet widely applied to study the SCI, may prove to be a valuable tool for characterising moisture distribution. Certainly, further studies are required to demonstrate, optimise and validate the use of NMR for characterising the SCI. Here, innovative approaches are needed to overcome the limitations caused by iron as a paramagnetic metal. This may include using advanced computational techniques, e.g. [146], to correct for the distorted electrical field or modification of experimental design aspects such as the use of non-magnetic metals (e.g. copper or others) as substitute for steel reinforcement.

8 Conclusions

We evaluated over twenty methods for studying local characteristics of the steel–concrete interface (SCI) identified as the main parameters influencing corrosion initiation in previous reports by the RILEM TC 262-SCI. The key findings are:

- (a) The SCI is physically and chemically complex with time-dependent properties that vary over multiple length scales due to many interacting factors. None of the existing methods was deemed satisfactory on its own to provide a complete characterisation of the main parameters influencing corrosion initiation. Therefore, combination of different methodologies is required.
- (b) Several established techniques are available for direct quantitative characterisation of selected features, namely mill scale and rust layers on the steel surface, and the interfacial voids and microstructure of the cementitious matrix at the SCI. However, no proven techniques exist for in-situ characterisation of the moisture content, state and distribution, and electrolyte solution composition at the SCI. Yet, we consider these as the main factors influencing corrosion.
- (c) A significant limitation of many current established techniques is that they are destructive, and thus unsuitable for monitoring time-dependent changes at the SCI or field application on actual structures. Another challenge is the conflict between achieving a representative field of view and high spatial resolution, limiting characterisation to small specimens of the SCI that may not represent conditions in engineering structures.
- (d) We cannot yet reliably determine the location of corrosion initiation with respect to other features at the SCI. Conventional two-dimensional characterisation may lead to misinterpretation of the actual mechanism. Nevertheless, several three-dimensional techniques have emerged in recent years, and more work is needed to establish and exploit these for characterising the SCI fully.
- (e) More research is needed to establish new or improved protocols to achieve non-destructive and representative characterisation of the SCI without losing sensitivity or resolution. Considering the challenges and current limitations, the way forward is to combine complementary techniques operating at different principles and length scales with statistical methods of sampling and computational modelling.
- (f) Several promising techniques were identified, and we see immense potential in the further development and application of these for future research:
- Advanced electrochemical methods for characterising mill scale and rust layers.
 - FIB-SEM tomography for characterizing interfacial voids and concrete microstructure, potentially in combination with numerical modelling to provide an understanding of reactive mass transport processes.
 - X-ray imaging or bi-modal X-ray and neutron imaging for spatial and temporal characterisation of interfacial voids, concrete microstructure and moisture, and mill scale and rust layers.
 - Nuclear magnetic resonance (NMR) for characterising moisture distribution.

Acknowledgements We acknowledge the input provided by all TC members attending the discussions of the TC meetings on 10 October 2019 (London, UK), 6 July 2020 (online), 6 November 2020 (online), 12 January 2021 (online), and 12 January 2022 (online). Additionally, we acknowledge the unpublished results that were provided by Hong Wong from Imperial College London, UK (Fig. 8a), and Ueli Angst, Nicolas Ruffray and Zhidong Zhang from ETH Zurich, Switzerland (Fig. 12).

Declarations

Conflict of interest The authors declare that they have no conflict of interest.

Open Access This article is licensed under a Creative Commons Attribution 4.0 International License, which permits use, sharing, adaptation, distribution and reproduction in any medium or format, as long as you give appropriate credit to the original author(s) and the source, provide a link to the Creative Commons licence, and indicate if changes were made. The images or other third party material in this article are included in the article's Creative Commons licence, unless indicated otherwise in a credit line to the material. If material is not included in the article's Creative Commons licence and your intended use is not permitted by statutory regulation or exceeds the permitted use, you will need to obtain permission directly from the copyright holder. To view a copy of this licence, visit <http://creativecommons.org/licenses/by/4.0/>.

References

1. Angst UM et al (2017) The steel–concrete interface. *Mater Struct* 50(2):143



2. Angst UM et al (2019) The effect of the steel-concrete interface on chloride-induced corrosion initiation in concrete—a critical review by RILEM TC 262-SCI. *Mater Struct* 52:88
3. Li L, Sagues AA (2001) Chloride corrosion threshold of reinforcing steel in alkaline solutions—open-circuit immersion tests. *Corrosion* 57(1):19–28
4. Pillai RG, Trejo D (2005) Surface condition effects on critical chloride threshold of steel reinforcement. *ACI Mater J* 102(2):103–109
5. Ghods P (2010) Multi-scale investigation of the formation and breakdown of passive films on carbon steel rebar in concrete. Carleton University, Ottawa
6. Manera M et al (2008) Chloride threshold for rebar corrosion in concrete with addition of silica fume. *Corros Sci* 50(2):554–560
7. Mammoliti LT et al (1996) The influence of surface finish of reinforcing steel and pH of the test solution on the chloride threshold concentration for corrosion initiation in synthetic pore solutions. *Cem Concr Res* 26(4):545–550
8. Stefanoni M et al (2015) Local electrochemistry of reinforcement steel—distribution of open circuit and pitting potentials on steels with different surface condition. *Corros Sci* 98:610–618
9. Ghods P et al (2010) Electrochemical investigation of chloride-induced depassivation of black steel rebar under simulated service conditions. *Corros Sci* 52(5):1649–1659
10. P. Ghods et al (2009) Effect of surface condition on the chloride-induced depassivation of rebar in concrete. In 12th International Conference on Fracture (ICF), Ottawa, Canada
11. Care S et al (2008) Mechanical properties of the rust layer induced by impressed current method in reinforced mortar. *Cem Concr Res* 38(8–9):1079–1091
12. Ghods P et al (2011) Microscopic investigation of mill scale and its proposed effect on the variability of chloride-induced depassivation of carbon steel rebar. *Corros Sci* 53(3):946–954
13. Karadakis K et al (2016) Numerical investigation of the role of mill scale crevices on the corrosion initiation of carbon steel reinforcement in concrete. *J Electrochem Soc* 163(6):C306–C315
14. Stratmann M, Müller J (1994) The mechanism of the oxygen reduction on rust-covered metal substrates. *Corros Sci* 36(2):327–359
15. Stefanoni M et al (2020) The mechanism controlling corrosion of steel in carbonated cementitious materials in wetting and drying exposure. *Cem Concr Compos* 113:103717
16. Doi K et al (2020) Role of mill scale on corrosion behavior of steel rebars in mortar. *Corros Sci* 177:108995
17. Angst UM, Elsener B (2017) The size effect in corrosion greatly influences the predicted life span of concrete infrastructures. *Sci Adv* 3(8):e1700751
18. Jaffer SJ, Hansson CM (2009) Chloride-induced corrosion products of steel in cracked-concrete subjected to different loading conditions. *Cem Concr Res* 39(2):116–125
19. Aligizaki KK et al (2000) Analysis of iron oxides accumulating at the interface between aggregates and cement paste. *Cem Concr Res* 30(12):1941–1945
20. Poole AB, Sims I (2016) *Concrete petrography: a handbook of investigative techniques*, 2nd edn. CRC Press, London
21. Murkute P et al (2019) Production of corrosion-resistant 316L stainless steel clads on carbon steel using powder bed fusion-selective laser melting. *J Mater Process Technol* 273:116243
22. Wong HS et al (2010) On the penetration of corrosion products from reinforcing steel into concrete due to chloride-induced corrosion. *Corros Sci* 52(7):2469–2480
23. Pacheco J, Çopuroğlu O (2016) Quantitative energy-dispersive X-ray microanalysis of chlorine in cement paste. *J Mater Civ Eng* 28(1):04015065
24. Wong HS, Buenfeld NR (2006) Patch microstructure in cement-based materials: fact or artefact? *Cem Concr Res* 36(5):990–997
25. Zhang Z et al (2020) A laboratory investigation of cutting damage to the steel-concrete interface. *Cem Concr Res* 138:106229
26. Burke DP, Higginson RL (2000) Characterisation of multicomponent scales by electron back scattered diffraction (EBSD). *Scr Mater* 42(3):277–281
27. Marcotte TD (2001) Characterization of chloride-induced corrosion products that form in steel-reinforced cementitious materials. University of Waterloo, Waterloo, p 354
28. Marcotte TD, Hansson CM (2007) Corrosion products that form on steel within cement paste. *Mater Struct* 40(3):325–340
29. Poursae A, Hansson C (2007) Reinforcing steel passivation in mortar and pore solution. *Cem Concr Res* 37(7):1127–1133
30. Criado M et al (2013) Corrosion rate and corrosion product characterisation using Raman spectroscopy for steel embedded in chloride polluted fly ash mortar. *Mater Corros* 64(5):372–380
31. Criado M et al (2015) A Raman spectroscopy study of steel corrosion products in activated fly ash mortar containing chlorides. *Constr Build Mater* 96:383–390
32. Demoulin A et al (2010) The evolution of the corrosion of iron in hydraulic binders analysed from 46- and 260-year-old buildings. *Corros Sci* 52(10):3168–3179
33. Jiang BZ et al (2020) Micromechanical properties of steel corrosion products in concrete studied by nano-indentation technique. *Corros Sci* 163:108304
34. L'Hostis V et al (2013) Characterisation of the steel concrete interface submitted to chloride-induced-corrosion. *Mater Corros* 64(3):185–194
35. de Faria DLA et al (1997) Raman microspectroscopy of some iron oxides and oxyhydroxides. *J Raman Spectrosc* 28(11):873–878
36. Dubois F et al (2008) Raman mapping of corrosion products formed onto spring steels during salt spray experiments. A correlation between the scale composition and the corrosion resistance. *Corros Sci* 50(12):3401–3409
37. Neff D et al (2006) Raman imaging of ancient rust scales on archaeological iron artefacts for long-term atmospheric corrosion mechanisms study. *J Raman Spectrosc* 37(10):1228–1237
38. Ghods P et al (2012) Angle-resolved XPS study of carbon steel passivity and chloride-induced depassivation in simulated concrete pore solution. *Corros Sci* 58:159–167

39. Ghods P et al (2011) XPS depth profiling study on the passive oxide film of carbon steel in saturated calcium hydroxide solution and the effect of chloride on the film properties. *Appl Surf Sci* 257(10):4669–4677
40. Ghods P et al (2013) Nano-scale study of passive films and chloride-induced depassivation of carbon steel rebar in simulated concrete pore solutions using FIB/TEM. *Cem Concr Res* 47:55–68
41. Gunay HB et al (2013) Characterization of atomic structure of oxide films on carbon steel in simulated concrete pore solutions using EELS. *Appl Surf Sci* 274:195–202
42. Elsener B, Rossi A (2018) Passivation of steel and stainless steel in alkaline media simulating concrete. In: Wandelt K (ed) *Encyclopedia of interfacial chemistry*. Elsevier, Oxford, pp 365–375
43. Oliver WC, Pharr GM (1992) An improved technique for determining hardness and elastic modulus using load and displacement sensing indentation experiments. *J Mater Res* 7(6):1564–1583
44. Zhao Y et al (2012) A study of the elastic moduli of corrosion products using nano-indentation techniques. *Corros Sci* 65:163–168
45. Šavija B et al (2015) Corrosion induced cover cracking studied by X-ray computed tomography, nanoindentation, and energy dispersive X-ray spectrometry (EDS). *Mater Struct* 48(7):2043–2062
46. Dehoux A et al (2015) Micromechanical and microstructural investigation of steel corrosion layers of variable age developed under impressed current method, atmospheric or saline conditions. *Corros Sci* 97:49–61
47. M. Serdar et al (2018) Micro-mechanical analysis of corrosion products formed during long-term carbonation induced corrosion of steel, in Sixth International Conference on Durability of Concrete Structures. Leeds. p 6
48. Stefanoni M et al (2019) Kinetics of electrochemical dissolution of metals in porous media. *Nat Mater* 18(9):942–947
49. Page CL (1975) Mechanism of corrosion protection in reinforced concrete marine structures. *Nature* 258:514–515
50. Garrett HL, Beaman DR (1985) A method for preparing steel reinforced mortar or concrete for examination by transmitted light microscopy. *Cem Concr Res* 15(5):917–920
51. Castel A et al (2003) Influence of steel–concrete interface quality on reinforcement corrosion induced by chlorides. *Mag Concr Res* 55(2):151–159
52. Soylev TA, François R (2003) Quality of steel–concrete interface and corrosion of reinforcing steel. *Cem Concr Res* 33(9):1407–1415
53. Zhang R et al (2011) Influence of steel–concrete interface defects owing to the top-bar effect on the chloride-induced corrosion of reinforcement. *Mag Concr Res* 63(10):773–781
54. Zhang X et al (2021) Applicability discussion for multi-peak Gaussian model of corrosion layer at steel/concrete interfaces. *Mater Struct* 54(2):55
55. Al Khalaf MN, Page CL (1979) Steel/mortar interfaces: microstructural features and mode of failure. *Cem Concr Res* 9(2):197–207
56. Yonezawa T et al (1988) Pore solution composition and chloride effects on the corrosion of steel in concrete. *Corrosion* 44(7):489–499
57. Gjorv OE et al (1990) Effect of condensed silica fume on the steel-concrete bond. *ACI Mater J* 87(6):573–580
58. Monteiro PJM et al (1985) Microstructure of the steel-cement paste interface in the presence of chloride. *Cem Concr Res* 15(5):781–784
59. Page CL (2009) Initiation of chloride-induced corrosion of steel in concrete: role of the interfacial zone. *Mater Corros* 60(8):586–592
60. Glass GK et al (2001) Backscattered electron imaging of the steel–concrete interface. *Corros Sci* 43(4):605–610
61. Wong HS, Buenfeld NR (2006) Euclidean distance mapping for computing microstructural gradients at interfaces in composite materials. *Cem Concr Res* 36(6):1091–1097
62. Horne AT et al (2007) Quantitative analysis of the microstructure of interfaces in steel reinforced concrete. *Cem Concr Res* 37(12):1613–1623
63. Wong HS, Buenfeld NR (2006) Monte Carlo simulation of electron–solid interactions in cement-based materials. *Cem Concr Res* 36(6):1076–1082
64. Yio MHN et al (2016) 3D Monte Carlo simulation of backscattered electron signal variation across pore–solid boundaries in cement-based materials. *Cem Concr Res* 89:320–331
65. Poupard O et al (2006) Corrosion damage diagnosis of a reinforced concrete beam after 40 years natural exposure in marine environment. *Cem Concr Res* 36(3):504–520
66. Koleva DA et al (2006) Quantitative characterisation of steel/cement paste interface microstructure and corrosion phenomena in mortars suffering from chloride attack. *Corros Sci* 48(12):4001–4019
67. Sugiyama T et al (2010) Application of synchrotron microtomography for pore structure characterization of deteriorated cementitious materials due to leaching. *Cem Concr Res* 40(8):1265–1270
68. Provis JL et al (2012) X-ray microtomography shows pore structure and tortuosity in alkali-activated binders. *Cem Concr Res* 42(6):855–864
69. Mac MJ et al (2021) 3D imaging techniques for characterising microcracks in cement-based materials. *Cem Concr Res* 140:106309
70. Yio MHN et al (2021) Effect of autogenous shrinkage on microcracking and mass transport properties of concrete containing supplementary cementitious materials. *Cem Concr Res* 150:106611
71. Maire E, Withers PJ (2014) Quantitative X-ray tomography. *Int Mater Rev* 59(1):1–43
72. Brisard S et al (2012) Morphological quantification of hierarchical geomaterials by X-ray nano-CT bridges the gap from nano to micro length scales. *Am Miner* 97(2–3):480–483
73. Davis GR, Elliott JC (2006) Artefacts in X-ray microtomography of materials. *Mater Sci Techn* 22:1011–1018
74. Mouton A et al (2013) An experimental survey of metal artefact reduction in computed tomography. *J X-Ray Sci Techn* 21:193–226
75. Brisard S et al (2020) Multiscale X-ray tomography of cementitious materials: a review. *Cem Concr Res* 128:105824



76. D Graham et al (2010) Quantitative X-ray microtomography with a conventional source. In: SPIE 7804, Developments in X-Ray Tomography VII. San Diego, California
77. Titarenko S et al (2010) A priori information in a regularized sinogram-based method for removing ring artefacts in tomography. *J Synchrotron Radiat* 17(4):540–549
78. Brooks RA, Di Chiro G (1976) Beam hardening in X-ray reconstructive tomography. *Phys Med Biol* 21(3):390
79. Cesen A et al (2013) Characterization of steel corrosion in mortar by various electrochemical and physical techniques. *Corros Sci* 75:47–57
80. Itty PA et al (2014) In situ 3D monitoring of corrosion on carbon steel and ferritic stainless steel embedded in cement paste. *Corros Sci* 83:409–418
81. Dong B et al (2017) Monitoring reinforcement corrosion and corrosion-induced cracking by X-ray microcomputed tomography method. *Cem Concr Res* 100:311–321
82. Van Steen C et al (2019) Localisation and characterisation of corrosion damage in reinforced concrete by means of acoustic emission and X-ray computed tomography. *Constr Build Mater* 197:21–29
83. Fang GH et al (2019) Identification of corrosion products and 3D distribution in reinforced concrete using X-ray micro computed tomography. *Constr Build Mater* 207:304–315
84. Rossi E et al (2020) The influence of defects at the steel/concrete interface for chloride-induced pitting corrosion of naturally-deteriorated 20-years-old specimens studied through X-ray Computed Tomography. *Constr Build Mater* 235:117474
85. Zhang P et al (2018) Application of neutron imaging to investigate fundamental aspects of durability of cement-based materials: a review. *Cem Concr Res* 108:152–166
86. Trtik P et al (2015) Improving the spatial resolution of neutron imaging at Paul Scherrer institute—the neutron microscope project. *Phys Procedia* 69:169–176
87. Trtik P, Lehmann EH (2016) Progress in high-resolution neutron imaging at the Paul Scherrer institute—the neutron microscope project. *J Phys Conf Ser* 746:012004
88. EO Garcez et al (2015) Durability in concrete: new instruments, new opportunities. In Proceedings of the 57th Congresso Brasileiro do Concreto. Brazil: IBRACON.
89. Garbe U et al (2017) Industrial Application Experiments on the Neutron imaging instrument DINGO. *Phys Procedia* 88:13–18
90. Zhang P et al (2018) 3D neutron tomography of steel reinforcement corrosion in cement-based composites. *Constr Build Mater* 162:561–565
91. C Boschmann Käthler (2019) Diss ETH Nr 26213 2019, ETH Zürich, Switzerland.
92. Robuschi S et al (2021) A closer look at corrosion of steel reinforcement bars in concrete using 3D neutron and X-ray computed tomography. *Cem Concr Res* 144:106439
93. L Holzer (2006) Quantification of capillary porosity in cement paste using high resolution 3D-microscopy: potential and limitations of FIB-nanotomography, In 2nd International RILEM Symposium on Advances in Concrete through Science and Engineering, J. Marchand, Editor. Quebec City, Canada
94. Holzer L et al (2006) FIB-Nanotomography of particulate systems—part I: particle shape and topology of interfaces. *J Am Ceram Soc* 89(8):2577–2585
95. Munch B et al (2006) FIB-nanotomography of particulate systems—part II: particle recognition and effect of boundary truncation. *J Am Ceram Soc* 89(8):2586–2595
96. Yio MH et al (2015) 3D imaging of cement-based materials at submicron resolution by combining laser scanning confocal microscopy with serial sectioning. *J Microsc* 258(2):151–169
97. N Ruffray (2020) From fresh concrete microstructure to digitally fabricated HPFRC: A challenging journey up from the nanoscale in search of precious digital macro-applications, ETH Diss. No. 26937. ETH Zurich, Switzerland
98. Yio MHN et al (2017) Representative elementary volume (REV) of cementitious materials from three-dimensional pore structure analysis. *Cem Concr Res* 102:187–202
99. L-O Nilsson (2018) Methods of measuring moisture in building materials and structures—State-of-the-Art Report of the RILEM Technical Committee 248-MMB. Springer, Cham
100. Geiker MR, Laugesen P (2001) On the effect of laboratory conditioning and freeze/thaw exposure on moisture profiles in HPC. *Cem Concr Res* 31(12):1831–1836
101. Linderoth O et al (2020) Development of pore structure, moisture sorption and transport properties in fly ash blended cement-based materials. *Constr Build Mater* 261:120007
102. Geiker M et al (2021) 25 years of field exposure of pre-cracked concrete beams; combined impact of spacers and cracks on reinforcement corrosion. *Constr Build Mater* 286:122801
103. Yang L et al (2015) In-situ tracking of water transport in cement paste using X-ray computed tomography combined with CsCl enhancing. *Mater Lett* 160:381–383
104. Bentz DP et al (2001) Shrinkage-reducing admixtures and early-age desiccation in cement pastes and mortars. *Cem Concr Res* 31(7):1075–1085
105. Oesch T et al (2019) Quantitative in-situ analysis of water transport in concrete completed using X-ray computed tomography. *Transp Porous Media* 127(2):371–389
106. Pease BJ et al (2012) Monitoring moisture movements in building materials using X-ray attenuation: Influence of beam-hardening of polychromatic X-ray photon beams. *Constr Build Mater* 36:419–429
107. Michel A, Pease BJ (2018) Moisture ingress in cracked cementitious materials. *Cem Concr Res* 113:154–168
108. Yang F et al (2016) Visualization of water drying in porous materials by X-ray phase contrast imaging. *J Microsc* 261(1):88–104
109. Justnes H et al (1994) Neutron radiography: an excellent method of measuring water penetration and moisture distribution in cementitious materials. *Adv Cem Res* 6(22):67–72
110. Brew DRM et al (2009) Water transport through cement-based barriers—a preliminary study using neutron radiography and tomography. *Nucl Instrum Methods Phys Res Sect A Accel Spectrom Detect Assoc Equip* 605(1):163–166

111. Zhang P et al (2011) Neutron radiography, a powerful method to determine time-dependent moisture distributions in concrete. *Nucl Eng Des* 241(12):4758–4766
112. Trtik P et al (2011) Release of internal curing water from lightweight aggregates in cement paste investigated by neutron and X-ray tomography. *Nucl Instrum Methods Phys Res Sect A Accel Spectrom Detect Assoc Equip* 651(1):244–249
113. Lucero CL et al (2015) Using neutron radiography to quantify water transport and the degree of saturation in entrained air cement based mortar. *Phys Procedia* 69:542–550
114. Dauti D et al (2018) Analysis of moisture migration in concrete at high temperature through in-situ neutron tomography. *Cem Concr Res* 111:41–55
115. Khanzadeh Moradillo M et al (2019) Quantifying fluid filling of the air voids in air entrained concrete using neutron radiography. *Cem Concr Compos* 104:103407
116. Zhang P et al (2010) Neutron imaging of water penetration into cracked steel reinforced concrete. *Physica B Condens Matter* 405(7):1866–1871
117. Andrade C, Page CL (1986) Pore solution chemistry and corrosion in hydrated cement systems containing chloride salts—a study of cation specific effects. *Br Corros J* 21(1):49–53
118. Angst U et al (2009) Critical chloride content in reinforced concrete—a review. *Cem Concr Res* 39(12):1122–1138
119. Angst UM et al (2011) Chloride induced reinforcement corrosion: electrochemical monitoring of initiation stage and chloride threshold values. *Corros Sci* 53(4):1451–1464
120. Goni S, Andrade C (1990) Synthetic concrete pore solution chemistry and rebar corrosion rate in the presence of chlorides. *Cem Concr Res* 20(4):525–539
121. Hansson CM et al (2006) Macrocell and microcell corrosion of steel in ordinary Portland cement and high performance concretes. *Cem Concr Res* 36(11):2098–2102
122. Li L, Sagüés AA (2002) Chloride corrosion threshold of reinforcing steel in alkaline solutions—cyclic polarization behavior. *Corrosion* 58(4):305–316
123. Ghods P et al (2009) The effect of concrete pore solution composition on the quality of passive oxide films on black steel reinforcement. *Cem Concr Compos* 31(1):2–11
124. Aguirre-Guerrero AM et al (2016) Corrosion performance of blended concretes exposed to different aggressive environments. *Constr Build Mater* 121:704–716
125. U Angst, B Elsener (2015) Forecasting chloride-induced reinforcement corrosion in concrete—effect of realistic reinforcement steel surface conditions. In *International conference on concrete repair, rehabilitation and retrofitting*. Leipzig: CRC Press
126. L Michel, U Angst (2018) Towards understanding corrosion initiation in concrete—influence of local electrochemical properties of reinforcing steel. In *International conference on concrete repair, rehabilitation and retrofitting 2018*. Cape Town, South Africa: EDP Sciences
127. Hren M et al (2019) Characterization of stainless steel corrosion processes in mortar using various monitoring techniques. *Constr Build Mater* 221:604–613
128. Michel A et al (2013) Experimental investigation of the relation between damage at the concrete-steel interface and initiation of reinforcement corrosion in plain and fibre reinforced concrete. *Corros Sci* 77:308–321
129. Ghantous RM et al (2017) Effect of accelerated carbonation conditions on the characterization of load-induced damage in reinforced concrete members. *Mater Struct* 50(3):175
130. M Raupach et al (2005) Monitoring the moisture distribution in concrete structures. In: Alexander MG, Beushausen HD, Dehn F, Moyo P (eds) *Concrete, repair, rehabilitation and retrofitting*. CRC Press, Cape Town
131. C Driessen, M Raupach (2018) Investigations on the detectability of water intruding into bridge deck sealings by electrical resistivity measurements. In *International conference on concrete repair, rehabilitation and retrofitting*. Cape Town, South Africa: EDP Sciences
132. Driessen C et al (2020) SMART DECK: Monitoring des Feuchtegehalts und Kathodischer Korrosionsschutz des Bewehrungsstahls in Brückenfahrbahnen durch Zwischenschichten aus Textilbeton. *Bauingenieur* 90:96–104
133. M Buettner et al (1996) Electrical resistance tomography for imaging concrete structures. In *Proceedings Structural materials technology: an NDT conference*. San Diego: CRC Press
134. Karhunen K et al (2010) Electrical resistance tomography imaging of concrete. *Cem Concr Res* 40(1):137–145
135. A Asgharzadeh et al (2015) Electrical impedance tomography in concrete, in *International symposium non-destructive testing in civil engineering (NDT-CE)*. Berlin
136. Reichling K et al (2015) Determination of the distribution of electrical resistivity in reinforced concrete structures using electrical resistivity tomography. *Mater Corros* 66(8):763–771
137. Hallaji M et al (2015) Electrical resistance tomography to monitor unsaturated moisture flow in cementitious materials. *Cem Concr Res* 69:10–18
138. Watanabe A et al (2019) Non-destructive chemical analysis of water and chlorine content in cement paste using near-infrared spectroscopy. *Constr Build Mater* 196:95–104
139. Soutsos MN et al (2001) Dielectric properties of concrete and their influence on radar testing. *NDT and E Int* 34(6):419–425
140. Laurens S et al (2005) Non-destructive evaluation of concrete moisture by GPR: experimental study and direct modeling. *Mater Struct* 38(9):827–832
141. Klysz G, Balayssac JP (2007) Determination of volumetric water content of concrete using ground-penetrating radar. *Cem Concr Res* 37(8):1164–1171
142. Klewe T et al (2021) Review of moisture measurements in civil engineering with ground penetrating radar—applied methods and signal features. *Constr Build Mater* 278:122250
143. Pérez-Gracia V et al (2008) Horizontal resolution in a non-destructive shallow GPR survey: an experimental evaluation. *NDT and E Int* 41(8):611–620
144. Rasol MA et al (2020) GPR laboratory tests and numerical models to characterize cracks in cement concrete specimens, exemplifying damage in rigid pavement. *Measurement* 158:107662



145. Wolter B, Krus M (2005) Moisture measuring with nuclear magnetic resonance (NMR). In: Kupfer K (ed) *Electromagnetic aquametry*. Springer, Berlin, pp 491–515
146. Schulte Holthausen R, Raupach M (2019) A phenomenological approach on the influence of paramagnetic iron in cement stone on 2D T1–T2 relaxation in single-sided 1H nuclear magnetic resonance. *Cem Concr Res* 120:279–293
147. Ebell G et al (2016) Investigation of chloride-induced pitting corrosion of steel in concrete with innovative methods. *Mater Corros* 67(6):583–590
148. Samson E, Marchand J (2007) Modeling the transport of ions in unsaturated cement-based materials. *Comput Struct* 85(23):1740–1756
149. Jensen MM et al (2014) Framework for reactive mass transport: phase change modeling of concrete by a coupled mass transport and chemical equilibrium model. *Comput Mater Sci* 92:213–223
150. Zhang Z et al (2015) Numerical modelling of moisture transfers with hysteresis within cementitious materials: verification and investigation of the effects of repeated wetting–drying boundary conditions. *Cem Concr Res* 68:10–23
151. Isgor OB, Weiss WJ (2018) A nearly self-sufficient framework for modelling reactive-transport processes in concrete. *Mater Struct* 52(1):3
152. Zhang Z, Angst U (2020) Modeling anomalous moisture transport in cement-based materials with kinetic permeability. *Int J Mol Sci* 21(3):837
153. Furcas FE et al (2022) Solubility and speciation of iron in cementitious systems. *Cem Concr Res* 151:106620

Publisher's Note Springer Nature remains neutral with regard to jurisdictional claims in published maps and institutional affiliations.

